

## Quarterly Technical Report

## Solid State Research

1987:1

---

### Lincoln Laboratory

MASSACHUSETTS INSTITUTE OF TECHNOLOGY

LEXINGTON, MASSACHUSETTS



---

Prepared under Electronic Systems Division Contract F19628-85-C-0002.

Approved for public release; distribution unlimited.

ADA 187893



The work reported in this document was performed at Lincoln Laboratory, a center for research operated by Massachusetts Institute of Technology, with the support of the Department of the Air Force under Contract F19628-85-C-0002.

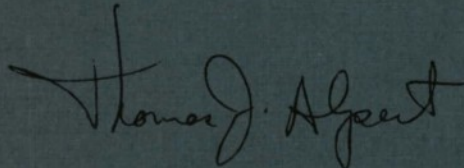
This Report may be reproduced to satisfy needs of U.S. Government agencies.

The views and conclusions contained in this document are those of the contractor and should not be interpreted as necessarily representing the official policies, either expressed or implied, of the United States Government.

The ESD Public Affairs Office has reviewed this report, and it is releasable to the National Technical Information Service, where it will be available to the general public, including foreign nationals.

This technical report has been reviewed and is approved for publication.

FOR THE COMMANDER

A handwritten signature in dark ink, appearing to read "Thomas J. Alpert". The signature is fluid and cursive, with the first name "Thomas" and last name "Alpert" clearly legible.

Thomas J. Alpert, Major, USAF  
Chief, ESD Lincoln Laboratory Project Office

Non-Lincoln Recipients

**PLEASE DO NOT RETURN**

Permission is given to destroy this document  
when it is no longer needed.

**MASSACHUSETTS INSTITUTE OF TECHNOLOGY  
LINCOLN LABORATORY**

**SOLID STATE RESEARCH**

**QUARTERLY TECHNICAL REPORT**

**1 NOVEMBER 1986 — 31 JANUARY 1987**

**ISSUED 15 JULY 1987**

**Approved for public release; distribution unlimited.**

**LEXINGTON**

**MASSACHUSETTS**

## **ABSTRACT**

This report covers in detail the solid state research work of the Solid State Division at Lincoln Laboratory for the period 1 November 1986 through 31 January 1987. The topics covered are Solid State Device Research, Quantum Electronics, Materials Research, Microelectronics, and Analog Device Technology. Funding is provided primarily by the Air Force, with additional support provided by the Army, DARPA, Navy, SDIO, NASA, and DOE.



# TABLE OF CONTENTS

Abstract	iii
List of Illustrations	vii
Introduction	xiii
Reports on Solid State Research	xv
Organization	xxiii
 1. SOLID STATE DEVICE RESEARCH	 1
1.1 High-Spectral-Purity CW and Pulsed Output from an Ensemble of Discrete Diode Lasers	1
1.2 Ohmic Heating in p-Substrate Buried-Heterostructure Lasers — An Analytical Solution	5
1.3 Proton Irradiation and Annealing of Fe-Doped Semi-insulating InP	10
1.4 16-Gb/s Large-Signal Digital Modulation of Diode Lasers	14
 2. QUANTUM ELECTRONICS	 19
2.1 Studies of Transient Effects in Ti:Al <sub>2</sub> O <sub>3</sub> Laser Tuning	19
2.2 Acousto-optic Modulator as a Unidirectional Device in a Ring Laser	22
2.3 Mode-Locked Ti:Al <sub>2</sub> O <sub>3</sub> Laser	25
2.4 Injection-Locking a 1.32- $\mu$ m Nd:YAG Laser with a Diode Laser	26
2.5 Generation of Second Harmonic of Nd:YAG Laser Radiation	28
 3. MATERIALS RESEARCH	 33
3.1 New System for Zone-Melting Recrystallization of SOI Films	33
3.2 Diffusion Model for Estimating Interface Widths in Heterostructures Grown in a Vertical OMVPE Reactor	35
 4. MICROELECTRONICS	 41
4.1 Laser-Direct-Written Tungsten Microstrip Lines for GaAs Monolithic Microwave Integrated Circuit Trimming	41
4.2 Small-Signal Gain Performance of the Permeable-Base Transistor at EHF	45
4.3 PBT Sample-and-Hold Circuits	48
4.4 Fabrication of Submicrometer-Size Structures in Si Using SF <sub>6</sub> /O <sub>2</sub> Reactive Ion Etching	51

5. ANALOG DEVICE TECHNOLOGY	57
5.1 Incremental Writing in MNOS Capacitors	57
5.2 Laser Photochemical Processing of Cr-Cr <sub>2</sub> O <sub>3</sub> Films for Amplitude Compensation of Surface-Acoustic-Wave Devices	60
5.3 Low-Phase-Noise Oscillators Stabilized by Bulk-Acoustic-Wave Holographic-Grating Resonators	63

## LIST OF ILLUSTRATIONS

Figure No.		Page
1-1	Schematic of Multiple-Element External-Cavity Arrangement Showing Placement of Five AR-Coated Diode Lasers, Associated Collimating Optics, Two Lenses, Spatial Filter, and End Mirror. As Indicated, Elements Are Separated by Focal Length of Lenses So Light Undergoes a Fourier Transform Four Times During One Round-Trip through Cavity.	1
1-2	Fabry-Perot Scanning-Spectrum-Analyzer Trace of Output from Multiple-Element External-Cavity System with Spatial Filter in Place. Top Trace Covers One Free Spectral Range Showing that There Are No Other Spectral Lines. Lower Trace on Expanded Scale Shows Linewidth Limited by 7.5-MHz Instrument Resolution.	2
1-3	Spectra of Pulse Output for External Cavity as Measured Using Fabry-Perot Scanning-Interferometer Spectrum Analyzer. Alternate Gain Elements (1, 3, and 5) Operated CW. Two Intermediate Gain Elements Pulsed from CW Bias. (a) Pulse Operation When Bias Is Set So External-Cavity Laser Is Just Above Threshold CW. (b) Pulse Operation When Bias Is Set So Laser Ensemble Is Well Below Threshold CW. Envelope of Pulses Indicates Linewidth (Pulse Rate Faster than Fabry-Perot Scan).	4
1-4	(a) Transverse Cross-Sectional View of a p-Substrate Mass-Transported GaInAsP/InP BH Laser. (b) Calculated Current and Voltage Distributions in Substrate	6
1-5	Thin Stream of Heat Flow Used in Calculation of Temperature $T(v,0)$ Along V-Axis (cf. Figure 1-4). Line Segment from $u = -W$ to $u = W$ Represents Laser Active Region.	7
1-6	Calculated Temperature Rise of Active Region Due to Ohmic Heating in p-Type Substrate When Device Is Mounted Junction-Side Up on Heatsink.	9
1-7	Resistivity vs Accumulated Dose for Several InP:Fe Crystals Irradiated with 100-keV Protons	11
1-8	Resistivity vs Anneal Temperature for InP:Fe Samples Irradiated with $3 \times 10^{14}$ - and $3 \times 10^{15}$ -cm <sup>-2</sup> 100-keV Protons	13



Figure No.		Page
1-9	Schematic of 16-Gb/s Digital Word Generator. Words Are Synthesized by Combining Appropriately Delayed Pulses from Four Comb Generators.	14
1-10	16-Gb/s Digital Modulation of a Laser Biased for a -3-dB Frequency of 16 GHz. Top Trace Corresponds to Detected Signal. Bottom Trace Corresponds to Electrical Drive. Time Scale Is 100 ps/div.	16
2-1	Cavity Layout of Electro-optically Tuned $\text{TiAl}_2\text{O}_3$ Laser	20
2-2	Tuning Response to a Triangular-Wave Drive Voltage: (a) Only $\text{LiNbO}_3$ Crystal in Cavity; (b) $\text{LiNbO}_3$ Crystal and Optical Bias Plate in Cavity	21
2-3	Cavity Used for Obtaining Single-Frequency and Mode-Locked Operation of a Unidirectional Ring $\text{Ti:Al}_2\text{O}_3$ Laser. Single-Frequency Operation Is Obtained with No Voltage Applied to AOM3 and 12 to 50 MHz Applied to AOM2. Mode-Locked Operation Is Obtained by Applying 120 MHz to AOM3 in Addition.	22
2-4	Spatial Profile of Laser Beam with and without an Acousto-optic Modulator for Acoustic Frequencies of (a) 22.8 and (b) 48.1 MHz. A First-Order Diffraction Peak Is Observed in Wings of Laser Beam.	24
2-5	Injection-Locking of a 1.32- $\mu\text{m}$ Nd:YAG Laser with a Diode Laser	27
2-6	Temporal Pulse Shape of an $\sim 100\text{-}\mu\text{s}$ Macropulse (20 ns/div) from a Nd:YAG Laser	28
2-7	SHG Efficiency vs Incident Power Density from a Nd:YAG Laser for a 25-mm-long $\text{LiIO}_3$ Crystal. Depletion Curve Is Calculated Based on Initial Slope of Data.	30
2-8	SHG Efficiency vs Incident Power Density Curves for Nd:YAG Macropulse Rate of 1.25 and 10 Hz	30
3-1	External View of New System for ZMR of SOI Films	34
3-2	Top View of Interior of New ZMR System	34
3-3	Calculated and "Measured" Interface Widths in $\text{SF}_6$ Tracer Gas Studies, Plotted as a Function of Flow Rate for Inlet-Susceptor Distances of 4 and 16 cm	38

Figure No.		Page
3-4	Interface Width in GaAs/AlGaAs Heterostructures Calculated as a Function of Hydrogen Flow Rate for Inlet-Susceptor Distance of 16 cm, Growth Rate of 10 Å/s, and Diffusivity Range for Trimethylgallium and Trimethylaluminum in Hydrogen	38
4-1	SEM of Laser-Direct-Written W Lines. (a) Connection of a W Line to Ti-Au Metallization. (b) W Film Conforming to an Etched Step on GaAs Substrate	43
4-2	SEM of a W Open-Circuit Stub Connected to a Ti-Au Microstrip Line. Entire GaAs Substrate Except Area of Ti-Au Metallization Is Covered by a Polyimide Layer.	44
4-3	Measured $ S_{21} $ of Circuit Shown in Figure 4-2	44
4-4	Measured Small-Signal Scattering Parameters of PBT Embedded in a 50-Ω System. (a) $S_{11}$ and $S_{22}$ with a 50-Ω Normalization Impedance. (b) $ S_{12} $ and $ S_{21} $ in Decibels	46
4-5	PBT Amplifier Circuit Embedded in EHF Mount	47
4-6	Small-Signal Gain Performance of a Single-Stage PBT Amplifier. Substrate and Mount Losses Have Been Removed from Data.	47
4-7	Circuit Schematic and Coplanar-Waveguide Layout for PBT Sample-and-Hold Circuit	49
4-8	Sample-and-Hold Measurement System	49
4-9	PBT Sample-and-Hold Circuit Schematic with Input Signal, Output Signal, and Sample Pulses	50
4-10	Measured Output Signal for PBT Sample-and-Hold for 2-, 4-, and 5-GHz Input Signal	50
4-11	Etch Rates of Si and SiO <sub>2</sub> as a Function of O <sub>2</sub> Concentration in Etching System. System Pressure and dc Bias Voltages Are Indicated.	51
4-12	Si Etch Profiles for Several SF <sub>6</sub> /O <sub>2</sub> Mixtures	53
4-13	SEM of a Grating with 100-nm Lines and 220-nm Spaces Etched in Si	54
5-1	Flatband-Voltage Shift $\Delta V_{FB}$ Plotted as a Function of Signal-Charge Packet. Leftmost Curve Is Obtained when Device Is Erased to a Known State and Written with a Signal-Charge Packet $Q_{1A}$ ,	

Figure No.		Page
	$Q_{1B}$ , $Q_{1C}$ , $Q_{1D}$ , $Q_{1E}$ , and $Q_{1F}$ . Remaining Curves Result from Incremental Writing and Show Flatband-Voltage Shift Plotted as a Function of Second Charge Packet, $Q_{2A}$ , $Q_{2B}$ , $Q_{2C}$ , $Q_{2D}$ , $Q_{2E}$ , and $Q_{2F}$ , Plotted on Displaced Abscissas with Origins at Corresponding First-Packet Size	58
5-2	Fat Zero $\Delta Q$ of Second-Writing Operation as a Function of First Signal-Charge Packet. Fat Zeros Represent Displacement of Second-Write Curves in Figure 5-1 from First-Write Curves.	59
5-3	Dc Sheet Resistance of Cermet (Film 1) Laser-Modified in $O_2$ Ambient for Selected Range of Total Gas Pressure within Reaction Cell. Insert Depicts Measurement Technique. Ohmic Pads Are Separated by 6.2 mm. Dc Sheet Resistance Prior to Laser Processing Is $2\text{ M}\Omega/\square$ .	61
5-4	Calculated Attenuation and Phase Shift of a SAW as a Function of RF Resistivity of a Massless Thin Film Deposited on YZ-LiNbO <sub>3</sub> and Measured Properties of Cermet Films. Dc Resistance of Film 1 Is Indicated; of Film 2 Is Inferred from Acoustic Properties.	62
5-5	Schematic of Circuit to Demonstrate BAW-Resonator-Stabilized Oscillator. Configuration Used to Measure Open-Loop Response Is Indicated.	64
5-6	Results of Preliminary Measurements of Phase Noise in BAW-Resonator-Stabilized Oscillators. Shown Is Noise in a Typical SAW Oscillator Multiplied to 1-GHz Operation and Noise for HBAR Devices. Also Shown Is a Theoretical Curve which Ignores Flicker-Noise Contributions from Either Circuit or Device, Obtained by Using Equation (5-1) with $G = 47\text{ dB}$ , $F = 4\text{ dB}$ , $P_c = 17\text{ dBm}$ , and $Q = 1.2 \times 10^4$ . Agreement Between Theory and Experiment Is Excellent. Bottom Curve Shows Projected Noise with Improvements Discussed in Text, Using Equation (5-1) with $G = 27\text{ dB}$ , $F = 4\text{ dB}$ , $P_c = 27\text{ dBm}$ , and $Q = 3 \times 10^4$ .	65
5-7	Standard Feedback-Oscillator Model Used to Calculate Phase Noise. To Measure Open-Loop Frequency Response $Ae^{j\phi}$ , Loop Is Broken as Shown in Figure 5-5 and a Test Signal Injected.	66
5-8	Results of Model Calculations of Phase Noise Compared with Measurements, Using Model of Figure 5-7 and Measured Open-Loop Response. Agreement Is within Measurement Accuracy of $\pm 4\text{ dBc/Hz}$ .	66



# INTRODUCTION

## 1. SOLID STATE DEVICE RESEARCH

The spectrum of the output from an external-cavity laser containing five discrete diode lasers operating as a coherent ensemble has been shown to correspond to a single mode of the cavity with very narrow linewidth. Both for CW operation and for pulsed operation above a low-level CW baseline, the linewidth is within the 7.5-MHz measurement resolution; for pulsed operation with no CW output, the linewidth is 9 MHz.

An analysis has been carried out for the ohmic heating in the p-type substrate of a mass-transported GaInAsP/InP buried-heterostructure laser mounted junction-side up on a heatsink. A simple analytical solution has been derived that is valuable for device design and diagnosis.

The electrical behavior of proton-irradiated semi-insulating InP:Fe has been studied as a function of proton dose and bulk Fe concentration. Changes in resistivity with proton dose are attributed to the production of both deep-acceptor and deep-donor levels, with the former found to anneal out faster.

A p-type-substrate mass-transported diode laser with minimal parasitic capacitance has been operated at a rate of 16 Gb/s under large-signal modulation conditions. The light output of the laser closely replicates the electrical drive signal synthesized by a special word generator constructed from four comb generators.

## 2. QUANTUM ELECTRONICS

Transient tuning experiments have been initiated on a Ti:Al<sub>2</sub>O<sub>3</sub> laser with a LiNbO<sub>3</sub> intracavity electro-optic tuner. Quasi-continuous tuning over 20 nm has been achieved with a 0.5-nm resolution.

An acousto-optic modulator has been used as a unidirectional element in dye and Ti:Al<sub>2</sub>O<sub>3</sub> ring lasers. The modulator has very low insertion loss in the laser cavity, can be used to operate the ring in either direction, and because of the unidirectional operation, eliminates spatial hole-burning in the gain medium.

A mode-locked Ti:Al<sub>2</sub>O<sub>3</sub> laser has generated 150-ps laser pulses. A Lyot filter and etalon in the ring laser cavity result in transform-limited laser pulses with an average power of 70 mW.

A Q-switched 1.32  $\mu$ m Nd:YAG laser has been injection-locked using the tunable output of a GaInAsP diode laser. Approximately 1 to 10 nW of diode laser radiation was found adequate to injection-lock a 1-W average power Nd:YAG laser.

Generation of the second harmonic of Nd:YAG laser radiation has been achieved with efficiencies greater than 50 percent by using LiIO<sub>3</sub>, and an average power of more than 5 W of 532-nm radiation has been obtained.

## 3. MATERIALS RESEARCH

A new system with better temperature control has been constructed for zone-melting recrystallization of Si-on-insulator films. Use of this system permits reproducible preparation of uniformly

recrystallized 4-in-diam. films and has also led to a significant improvement in the quality of films less than  $0.5\text{ }\mu\text{m}$  thick.

A one-dimensional diffusion model has been developed for calculating the dispersion of reactant gases along the length of a vertical reactor tube used for organometallic vapor-phase epitaxy. According to this model, which is consistent with the results of tracer gas experiments, interface widths on the order of a few monolayers can be obtained in GaAs/AlGaAs heterostructures grown at the rate of  $10\text{ }\text{\AA}/\text{s}$  in a reactor operating at a pressure of 0.1 atm.

#### 4. MICROELECTRONICS

Laser-direct-written tungsten lines have been added as open stubs to existing microstrip lines on GaAs substrates. These tungsten lines can provide fast, versatile, and damage-free tuning of GaAs monolithic microwave integrated circuits without the incorporation of any other prefabricated tuning structures.

A prototype permeable base transistor (PBT) amplifier achieved 11 dB of stable gain at 40.5 GHz. The circuit design was facilitated by the moderate impedance levels and highly unilateral nature of the PBT.

A sample-and-hold circuit has been fabricated using a PBT device as the switch. This circuit has been used to successfully sample a 5-GHz waveform.

Submicrometer-size features have been etched in silicon by adding  $\text{O}_2$  to  $\text{SF}_6$  in a reactive ion etching mode. High etch rates of 60 nm/min, aspect ratios greater than 6:1, and high selectivity to  $\text{SiO}_2$  have been achieved without detrimental sidewall polymerization.

#### 5. ANALOG DEVICE TECHNOLOGY

An investigation has been made of the use of MNOS capacitors as nonvolatile analog memory elements in associative neural-network circuits. Experiments have shown that such capacitors can accumulate successive samples of analog information in an incremental mode, with the accumulation following a relatively simple linear law.

Laser photochemical processing of  $\text{Cr-Cr}_2\text{O}_3$  films has been developed for the amplitude trimming of SAW devices. Conductive ( $2\text{-M}\Omega/\square$  dc surface resistivity) and highly acoustically attenuating (0.4 dB per acoustic wavelength) cermet films, when subjected to focused 488-nm laser radiation in a low-pressure  $\text{O}_2$  ambient, have been rendered insulating ( $>100\text{ M}\Omega/\square$ ) and non-attenuating (0.01 dB/ $\lambda$ ) with minimal change in phase characteristics.

Oscillators operating at 1 GHz have been built using holographic bulk-acoustic-wave reflection-grating resonators as the stabilization element and exhibit phase noise of  $-125\text{ dBc/Hz}$  at 10 kHz from the carrier. A model has been developed which gives good agreement with these measurements and predicts that this phase noise can be reduced to  $-170\text{ dBc/Hz}$  at 1 GHz and  $-130\text{ dBc/Hz}$  at 10 GHz.

# REPORTS ON SOLID STATE RESEARCH

1 November 1986 through 31 January 1987

## PUBLISHED REPORTS

### Journal Articles

#### JA No.

- |      |   |  |  |
|------|---|--|--|
| 5838 | Transient Transport Measurements on Ion Implanted Polymers  | B. Wasserman*<br>M.S. Dresselhaus*<br>M. Wolf*<br>J.D. Woodhouse<br>G.E. Wnek* | J. Appl. Phys. <b>60</b> , 668 (1986)                      |
| 5853 | A Comparison of Power Requirements of Traveling-Wave LiNbO <sub>3</sub> Optical Couplers and Interferometric Modulators | J.P. Donnelly<br>A. Gopinath   | IEEE J. Quantum Electron. <b>QE-23</b> , 30 (1987)         |
| 5854 | Fully Implanted p-Column InP Field-Effect Transistor  | J.D. Woodhouse<br>J.P. Donnelly  | IEEE Electron Device Lett. <b>EDL-7</b> , 387 (1986)       |
| 5859 | Observation of Gain Compression in a GaAlAs Diode Laser Through a Picosecond Transmission Measurement                   | B.C. Johnson<br>A. Mooradian   | Appl. Phys. Lett. <b>49</b> , 1135 (1986), DTIC AD-A176057 |
| 5872 | Laser Remote Sensing of the Atmosphere  | D.K. Killinger<br>N. Menyuk  | Science <b>235</b> , 37 (1987)                             |
| 5878 | Large Room-Temperature Effects from Resonant Tunneling Through AlAs Barriers  | W.D. Goodhue<br>T.C.L.G. Sollner<br>H.Q. Le<br>E.R. Brown<br>B.A. Vojak        | Appl. Phys. Lett. <b>49</b> , 1086 (1986), DTIC AD-A176071 |
| 5882 | Wideband Packet Radio Technology  | J.H. Fischer<br>J.H. Cafarella<br>D.R. Arsenault<br>G.T. Flynn<br>C.A. Bouman  | Proc. IEEE <b>75</b> , 100 (1987)                          |

---

\* Author not at Lincoln Laboratory.



**JA No.**

- |      |   |  |   |
|------|---|--|---|
| 5896 | Laser Photochemical Etching of Molybdenum and Tungsten Thin Films by Surface Halogenation   | M. Rothschild<br>J.H.C. Sedlacek<br>D.J. Ehrlich | Appl. Phys. Lett. <b>49</b> , 1554 (1986) |
| 5922 | High-Spectral-Purity cw and Pulse Output ( $\Delta f < 10$ MHz) from an External-Cavity-Controlled Array of Discrete Diode Lasers | K.A. Anderson<br>R.H. Rediker                    | Appl. Phys. Lett. <b>50</b> , 1 (1987)    |

**Meeting Speeches****MS No.**

- |      |  |   |   |
|------|--|---|---|
| 7094 | A Comparison of Neural-Network and Matched-Filter Processing for Detecting Lines in Images | P.M. Grant<br>J.P. Sage   | AIP Conference Proceedings, Vol. 151, <i>Neural Networks for Computing</i> , Snowbird, Utah, 13-16 April 1986, pp. 194-199  |
| 7095 | A Neural-Network Integrated Circuit with Synapses Based on CCD/MNOS Principles             | J.P. Sage<br>K.E. Thompson<br>R.S. Withers  | AIP Conference Proceedings, Vol. 151, <i>Neural Networks for Computing</i> , Snowbird, Utah, 13-16 April 1986, pp. 381-385  |
| 7126 | Growth of GaAs on Si   | G.W. Turner   | <i>Semiconductor-Based Heterostructures: Interfacial Structure and Stability</i> , Proc. Northeast Regional Mtg. of Metallurgical Soc., Murray Hill, New Jersey, 1-2 May 1986, p. 235 |
| 7149 | Radiation-Hardened JFET Devices and CMOS Circuits Fabricated in SOI Films                  | B-Y. Tsaur<br>V.J. Sferri<br>H.K. Choi<br>C.K. Chen<br>R.W. Mountain<br>J.T. Schott*<br>W.M. Shedd*<br>D.C. LaPierre*<br>R. Blanchard | IEEE Trans. Nucl. Sci. <b>NS-33</b> , 1372 (1986)   |

---

\* Author not at Lincoln Laboratory.

**MS No.**

7160 Growth of  $\text{Ti:Al}_2\text{O}_3$  Crystals  
by a Gradient-Freeze Technique

R.E. Fahey  
A.J. Strauss  
A. Sanchez  
R.L. Aggarwal

*Tunable Solid State Lasers II*,  
Proc. Topical Mtg. on  
Tunable Solid State Lasers,  
ZigZag, Oregon, 4-6 June  
1986, Vol. 52, p. 82

\* \* \* \* \*

**UNPUBLISHED REPORTS****Journal Articles****JA No.**

5871 Symmetric Three-Guide Optical  
Coupler with Non-identical  
Center and Outside Guides

J.P. Donnelly  
H.A. Haus\*  
N. Whitaker

Accepted by IEEE J. Quan-  
tum Electron.

5903 Laser Photosublimation of  
Compound Semiconductors

M. Rothschild  
C. Arnone  
D.J. Ehrlich

Accepted by J. Mat. Res.

5925 Radiation-Hardened Silicon-  
on-Insulator Junction Field-  
Effect Transistors Fabricated  
by a Self-Aligned Process

H.K. Choi  
B-Y. Tsaur  
C.K. Chen

Accepted by Electron Device  
Lett.

5934 Use of Flow Visualization and  
Tracer Gas Studies for Design-  
ing an InP/InGaAsP OMVPE  
Reactor

S.C. Palmateer  
S.H. Groves  
C.A. Wang  
D.W. Weyburne\*  
R.A. Brown\*

Accepted by J. Cryst.  
Growth

5951 Large Monolithic Two-Dimen-  
sional Arrays of GaInAsP/InP  
Surface-Emitting Lasers

Z.L. Liao  
J.N. Walpole

Accepted by Appl. Phys.  
Lett.

---

\* Author not at Lincoln Laboratory.

## Meeting Speeches\*

### MS No.

7095B	An Artificial Neural Network Integrated Circuit Based on MNOS/CCD Principles	J.P. Sage	Seminar, GTE Laboratories, Waltham, Massachusetts, 14 January 1987
7095C	Associative Memories, Neural Networks, and the Hopfield Model	J.P. Sage	Seminar, General Motors Research Laboratories, Detroit, Michigan, 28 January 1987
7167A	Analog Signal Correlator Using Superconductive Integrated Components	R.W. Ralston	Superconducting Research Seminar, Electrotechnical Laboratory, Tsukuba, Japan, 11 December 1986
7354A	Analog Signal Processing for Superconductive Wideband Receivers	R.W. Ralston	
7178	A CCD Parallel Pulse-Doppler Radar Processor	A.M. Chiang	GOMAC, San Diego, California, 11-13 November 1987
7227C	The Fabrication and Performance of the Permeable Base Transistor	R.A. Murphy	Seminar, Los Alamos National Laboratory, New Mexico, 16 December 1986
7268	Emerging Technology for <i>In-Situ</i> Processing	D.J. Ehrlich	Materials Research Society, Boston, 1-4 December 1986
7269A	Etching with Directed Beams of Ions or Radicals	M.W. Geis N.N. Efremow G.A. Lincoln S.W. Pang	
7273	GaAs Circuit Restructuring by Multi-level Laser-Direct-Written Tungsten Process	J.G. Black S.P. Doran M. Rothschild J.H.C. Sedlacek D.J. Ehrlich	

---

\* Titles of Meeting Speeches are listed for information only. No copies are available for distribution.

# MS No.

7294	Elimination of Subboundaries in 0.5- $\mu$ m-Thick Si Film Produced by ZMR	M.W. Geis H.I. Smith* C.K. Chen	Materials Research Society, Boston, 1-4 December 1986
7274	Adaptive and Matched Filtering with a SAW/FET Programmable Transversal Filter	J.B. Green D.E. Oates P.M. Grant D.L. Smythe	IEEE 1986 Ultrasonics Symposium, Williamsburg, Virginia, 17-19 November 1986
7275	Bulk-Wave Reflection-Grating Devices	D.E. Oates	
7289	Self-Aligned SOI Junction Field-Effect Transistors	H.K. Choi B-Y. Tsaur C.K. Chen	1986 IEEE International Electron Devices Meeting, Los Angeles, 7-10 December 1986
7299	Monolithic Two-Dimensional GaInAsP/InP Laser Arrays	Z.L. Liao J.N. Walpole	
7315	Progress in Mass-Transported GaInAsP/InP Diode Laser Arrays	J.N. Walpole Z.L. Liao	Lasers '86, Orlando, Florida, 3-7 November 1986
7329	Microwave and Millimeter-Wave Resonant Tunneling Diodes	T.C.L.G. Sollner E.R. Brown W.D. Goodhue	2nd Topical Meeting on Picosecond Electronics and Optoelectronics, Incline Village, Nevada, 14-16 January 1987
7393	Picosecond Optoelectronic Switches Using Composite Electronic Materials	E.A. Chauchard* C.H. Lee* V. Diadiuk G.W. Turner	
7379	Laser and Electron-Stimulated Surface Reactions	D.J. Ehrlich	Electron Microscopy Workshop, Arizona State University, Tempe, 11-15 January 1987
7409	Charge-Coupled Devices for Image Processing	J.P. Sage	Lecture, Case Western Reserve University, Cleveland, Ohio, 20 November 1986

---

\* Author not at Lincoln Laboratory.



## ORGANIZATION

### SOLID STATE DIVISION

A.L. McWhorter, *Head*  
I. Melngailis, *Associate Head*  
E. Stern, *Associate Head*  
J.F. Goodwin, *Assistant*  
N.L. DeMeo, Jr., *Associate Staff*

### QUANTUM ELECTRONICS

A. Mooradian, *Leader*  
P.L. Kelley, *Associate Leader*

Aggarwal, R.L.	Le, H.Q.
Barch, W.E.	Menyuk, N.
Belanger, L.J.	Sanchez-Rubio, A.
Brailove, A.A.	Seppala, J.P.
Cali, C.	Schulz, P.A.
Daneu, V.	Sharpe, K.A.
DeFeo, W.E.	Sullivan, D.J.
Hancock, R.C.	Tong, F.F-K.*
Harrison, J.*	Wall, K.F.
Jeys, T.H.	Walker, W.A.
Killinger, D.K.	Walther, A.
Lacovara, P.	Zayhowski, J.J.

### ELECTRONIC MATERIALS

A.J. Strauss, *Leader*  
B-Y. Tsaur, *Assistant Leader*  
H.J. Zeiger, *Senior Staff*

Anderson, C.H., Jr.	Krohn, L., Jr.
Button, M.J.	Mastromattei, E.L.
Chen, C.K.	Mattia, J.P.
Choi, H.K.	Nitishin, P.M.
Connors, M.K.	Pantano, J.V.
Delaney, E.J.	Tracy, D.M.
Eglash, S.J.	Turner, G.W.
Fahey, R.E.	Wang, C.A.
Finn, M.C.	Windhorn, T.H.
Iseler, G.W.	Young, K.K.
Kolesar, D.F.	

### APPLIED PHYSICS

R.C. Williamson, *Leader*  
D.L. Spears, *Assistant Leader*  
T.C. Harman, *Senior Staff*  
R.H. Rediker, *Senior Staff*

Aull, B.F.	Groves, S.H.	Palmateer, S.C.
Betts, G.E.	Hovey, D.L.	Plonko, M.C.
Bossi, D.E.*	Johnson, L.M.	Reeder, R.E.
Chan, S.K.*	Liau, Z.L.	Tsang, D.Z.
Corcoran, C.J.*	Lind, T.A.	Walpole, J.N.
Cox, C.H., III	Metze, G.M.	Woodhouse, J.D.
Diadiuk, V.	Molter, L.A.*	Yap, D.*
Donnelly, J.P.	O'Donnell, F.J.	Yee, A.C.
Ferrante, G.A.	Palmacci, S.T.	

---

\* Research Assistant

## ANALOG DEVICE TECHNOLOGY

R.W. Ralston, *Leader*

R.S. Withers, *Associate Leader*

Anderson, A.C.  
Arsenault, D.R.  
Boisvert, R.R.  
Brogan, W.T.  
Denneno, A.P.  
DiIorio, M.S.  
Dolat, V.S.

Fitch, G.L.  
Frickey, J.M.  
Green, J.B.  
Holtham, J.H.  
Koulman, W.A.  
Lattes, A.L.  
Lichtenwalner, D.J.\*

Macedo, E.M., Jr.  
Munroe, S.C.  
Oates, D.E.  
Sage, J.P.  
Slattery, R.L.  
Thompson, K.E.†  
Wong, S.C.\*

## MICROELECTRONICS

W.T. Lindley, *Leader*

R.A. Murphy, *Associate Leader*

D.J. Ehrlich, *Assistant Leader*

B.B. Kosicki, *Assistant Leader*

Astolfi, D.K.  
Bales, J.W.\*  
Bennett, P.C.  
Black, J.G.  
Bozler, C.O.  
Brown, E.R.  
Burke, B.E.  
Calawa, A.R.  
Chen, C.L.  
Chiang, A.M.  
Clifton, B.J.  
Cullen, P.A.\*  
Daniels, P.J.  
Doherty, C.L., Jr.  
Doran, S.P.  
Durant, G.L.  
Efremow, N.N., Jr.  
Felton, B.J., Jr.

Gajar, S.A.\*  
Geis, M.W.  
Goodhue, W.D.  
Gray, R.V.  
Hollis, M.A.  
Huang, J.C.M.  
Johnson, K.F.  
LaFranchise, J.R.  
LeCoz, Y.L.\*  
Lincoln, G.A., Jr.  
Lyszczarz, T.M.  
Mahoney, L.J.  
Maki, P.A.  
Manfra, M.J.  
Mathews, R.H.  
McGonagle, W.H.  
McIntosh, K.A.  
Melngailis, J.†

Mountain, R.W.  
Nichols, K.B.  
Pang, S.W.  
Parker, C.D.  
Pichler, H.H.  
Rabe, S.  
Rathman, D.D.  
Reinold, J.H., Jr.  
Rothschild, M.  
Sedlacek, J.H.C.  
Smith, F.W.\*  
Smythe, D.L., Jr.  
Sollner, T.C.L.G.  
Utarro, R.S.  
Vera, A.  
Wilde, R.E.  
Young, E.M.

---

\* Research Assistant

† Staff Associate

‡ Part Time

# 1. SOLID STATE DEVICE RESEARCH

## 1.1 HIGH-SPECTRAL-PURITY CW AND PULSED OUTPUT FROM AN ENSEMBLE OF DISCRETE DIODE LASERS

Recently, five diode lasers with antireflection-coated end facets were controlled to operate as a coherent ensemble by a spatial filter within a common external cavity.<sup>1</sup> Here we report the results of experiments showing that high-spectral-output purity can be achieved from this ensemble in both CW and pulsed operation. Figure 1-1 shows the experimental arrangement including the five antireflection-coated GaAlAs, channel-substrate-planar (CSP) diode lasers at one end of the cavity structure. The collimated light from the elements, whose center-to-center spacing  $d$  is 1.98 cm, is incident upon a primary lens, whose focal length  $F$  is 25 cm. The light is then focused down to the focal plane of the lens where the spatial filter element is situated. After passing through the filter, which consists of a series of  $3.1\text{-}\mu\text{m}$  slits whose center-to-center spacing  $D$  is  $10.47\text{ }\mu\text{m}$ , the light is recollimated by a second lens and incident upon the partially reflecting end mirror. The reflected light then makes the round-trip through the cavity. For equal power from each gain element and for radiation of wavelength  $\lambda = D(d/F)$ , calculations predict a single-pass maximum transmission of 92 percent through the filter because the subsidiary maxima between the large peaks in the Fourier transform are blocked by the opaque stripes of the filter.

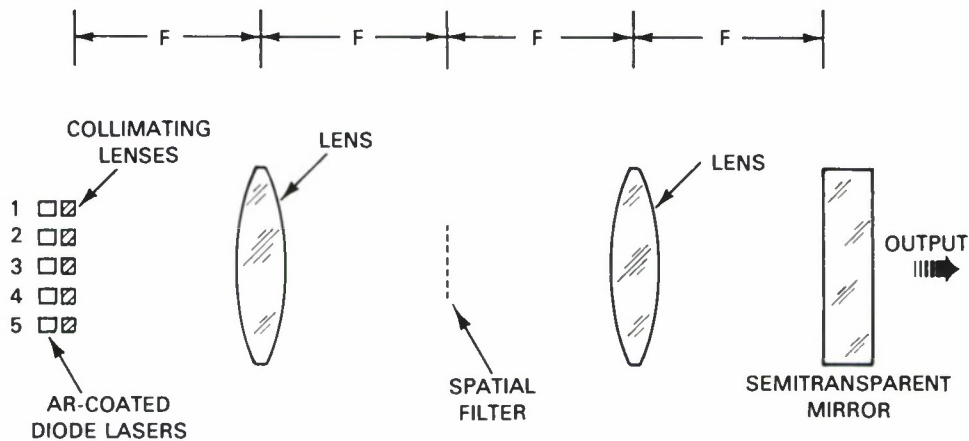


Figure 1-1. Schematic of multiple-element external-cavity arrangement showing placement of five AR-coated diode lasers, associated collimating optics, two lenses, spatial filter, and end mirror. As indicated, elements are separated by focal length of lenses so light undergoes a Fourier transform four times during one round-trip through cavity.

With no spatial filter in the cavity, each of the five elements operates independently as an external-cavity laser. The operating wavelengths of the individual lasers used in the experiments in this report are separated by more than  $60 \text{ \AA}$  (see Reference 1). With the spatial filter in place, output was measured on a 7.5-MHz ( $2.7 \times 10^{-4} \text{ \AA}$ ) resolution Tropel Model 240 Fabry-Perot scanning spectrum analyzer with 1.5-GHz ( $5.4 \times 10^{-2} \text{ \AA}$ ) free spectral range. Figure 1-2 is an oscilloscope display of the output from this instrument scanning one complete free spectral range. The top trace indicates the output is in a single spectral mode. As shown in the expanded scale of the lower trace, the linewidth is within the 7.5-MHz instrument resolution.

The external-cavity laser also has been operated in the pulse mode with output linewidths on the order of the 7.5-MHz instrument resolution. To achieve this high-spectral purity in a pulse mode, three alternate gain elements (1, 3, and 5 in Figure 1-1) are operated CW and the two intermediate elements are pulsed. For a coherent ensemble of only three alternate gain elements, the spacing between the major intensity maxima in the Fourier filter plane is decreased by a factor of two relative to the spacing with all five elements operating coherently. As a result, the lasing threshold for the three-element ensemble is much higher because significant radiation hits the opaque areas of the filter. A calculation of the single-pass filter transmission for this case yields a value of 0.48 as compared with the transmission of 0.92 when all five elements are running, as described above.

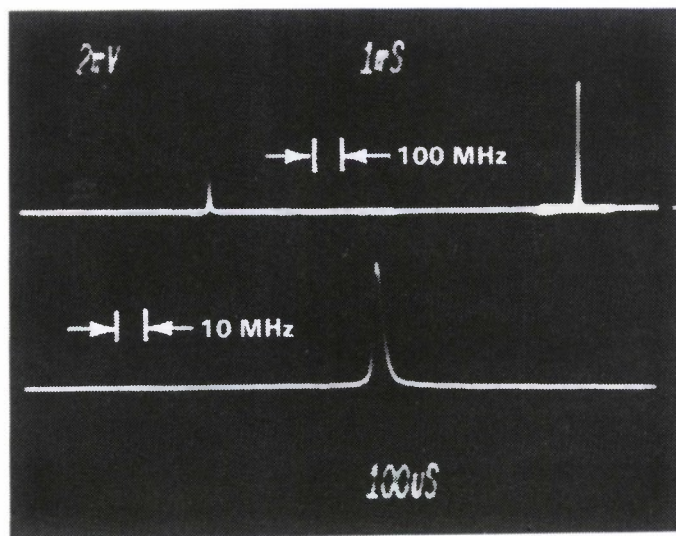


Figure 1-2. Fabry-Perot scanning-spectrum-analyzer trace of output from multiple-element external-cavity system with spatial filter in place. Top trace covers one free spectral range showing that there are no other spectral lines. Lower trace on expanded scale shows linewidth limited by 7.5-MHz instrument resolution.



The spectral output of the ensemble when operated with current pulses applied to elements 2 and 4, and CW excitation to the other three, was measured for two different cases. First, the dc biases on the two pulsed elements were set so the laser ensemble was just above threshold when the pulse was off. In this case, the spectrum for the pulse output remains at the value set by the low-level CW output of the external cavity and the resulting spectrum, shown in Figure 1-3(a), is a single-spectral mode. Note that in interpreting Figure 1-3(a), the time for one Fabry-Perot scan is much longer than the pulse repetition time, and the envelope of the pulses indicates the linewidth. The linewidth in this case is within the 7.5-MHz instrument resolution. It should be pointed out that if any of the five external-cavity lasers operating independently without the spatial filter are pulsed from below threshold, there is a  $1\text{-}\text{\AA}$  ( $\approx 40\text{-GHz}$ ) output-frequency shift (chirp) during the pulse, and there is still a chirp larger than 1.5 GHz if all five elements of the coherent ensemble with the spatial filter are pulsed simultaneously from above the ensemble threshold.

For the second case, the dc biases on the two pulsed elements were reduced to a point where the ensemble was well below threshold with the pulse off. The spectrum for this case is again a single spectral mode, shown in Figure 1-3(b), with an apparent linewidth of 9 MHz. Again, for the results shown in Figure 1-3(b), the time for one Fabry-Perot scan is much longer than the pulse repetition time. In this case there is no Fabry-Perot output when the pulse is off.

The narrow linewidth pulses can be explained by a compensation effect. Refractive index and gain in pulsed elements 2 and 4 change because of increased temperatures and carriers caused by the increased current. In the other three elements, however, changes occur in the opposite direction because of decreased temperatures and carriers caused by the increase in coherently emitted power output and the simultaneous decrease in carrier lifetime. Since the measured linewidths of all the spectra shown in this report are less than or close to the specification of the instrument resolution, the actual linewidths cannot be quantified accurately.

K.K. Anderson

R.H. Rediker

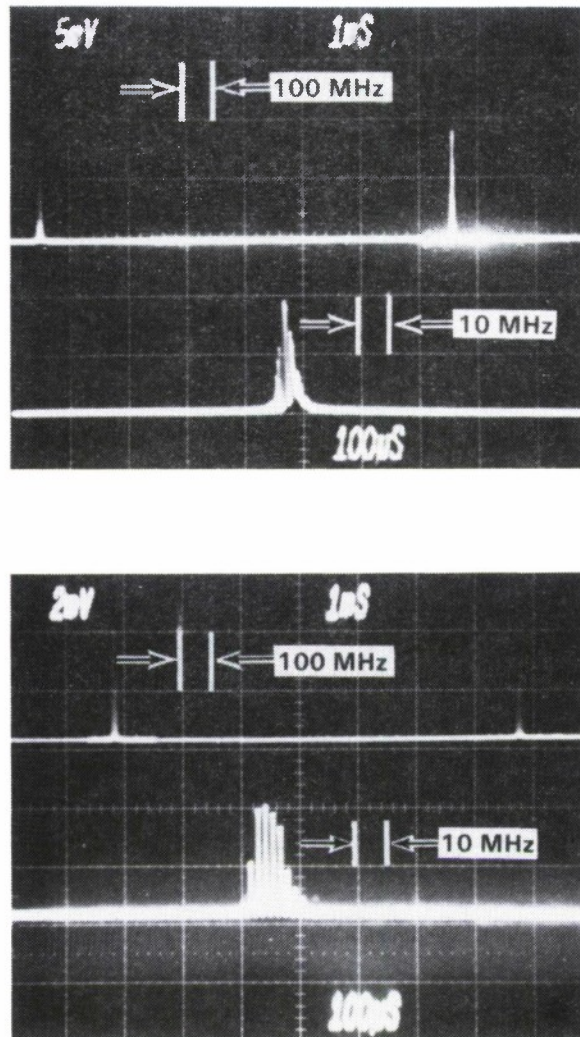


Figure 1-3. Spectra of pulse output for external cavity as measured using Fabry-Perot scanning-interferometer spectrum analyzer. Alternate gain elements (1, 3, and 5) operated CW. Two intermediate gain elements pulsed from CW bias. (a) Pulse operation when bias is set so external-cavity laser is just above threshold CW. (b) Pulse operation when bias is set so laser ensemble is well below threshold CW. Envelope of pulses indicates linewidth (pulse rate faster than Fabry-Perot scan).

## 1.2 OHMIC HEATING IN P-SUBSTRATE BURIED-HETEROSTRUCTURE LASERS — AN ANALYTICAL SOLUTION

One of the potential advantages of the recently developed p-substrate GaInAsP/InP buried-heterostructure (BH) lasers is better heatsinking when the device is mounted junction-side up on a heatsink. This is because the two dominant resistive heat sources, the p-type contact and the p-InP, are closer to the heatsink and will cause less temperature rise at the active region. For a more quantitative assessment, we have carried out an analysis of the ohmic heating in the p-InP substrate and have obtained a simple analytical solution.

Figure 1-4 shows schematic cross-sectional views of a mass-transported BH laser (a), together with the substrate current and voltage distributions (b) derived in our previous report.<sup>2</sup> The ohmic heat generated by the current flow in the p-substrate can be analyzed accurately using these distributions. To obtain a simple solution for the resulting temperature rise in the laser active region, we assume that the heat flow follows the same boundary conditions as the electrical current, i.e., the p-contact and the active region are both isotherms and no heat flows across the sidewalls. Note that this assumption is a good approximation for the present device mounted junction-side up on a heatsink.

It can then be shown that the heat flow follows the same set of streamlines as the electric current. This can be seen by dividing the substrate into many *very small* rectangular regions by using equipotentials and streamlines of equal increments of voltage and current, respectively. All the small rectangular regions generate the same amount of ohmic heat and are similar in shape (because  $\nabla^2 V = 0$ ). The increments of temperature gradient across these small regions are therefore the same; hence (by using the assumed boundary conditions), the equipotentials should become isotherms.

To calculate the temperature profile along the streamlines, we consider ohmic heat generation and its resulting flow in a long narrow region defined by a pair of streamlines near the v-axis (vertical axis of the device in Figure 1-4) as shown in Figure 1-5. The small width of the region  $\Delta u(0,v)$  is a function of  $v$  and is conveniently denoted as  $\Delta u(0,0) \equiv 2\epsilon$  at the origin (middle of the active region). Because  $\nabla^2 \Phi(u,v) = 0$ , we have from the divergence theorem

$$\Delta u(0,v) = 2\epsilon \frac{\partial \Phi}{\partial v}(0,0) / \frac{\partial \Phi}{\partial v}(0,v) \quad (1-1)$$

(The potential function  $\Phi(u,v)$  is the same as that defined previously<sup>2</sup> and is closely related to the voltage distribution, i.e.,  $V(u,v) = (\rho I / \pi L) \Phi(u,v) + \text{constant}$ , where  $\rho$ ,  $I$ , and  $L$  are the resistivity, current, and device length, respectively.)

The ohmic heat  $\Delta P$  generated per unit time in this region between  $v = 0$  and  $v = v$  is given by

$$\Delta P = \Delta I [V(0,v) - V(0,0)] \quad (1-2)$$

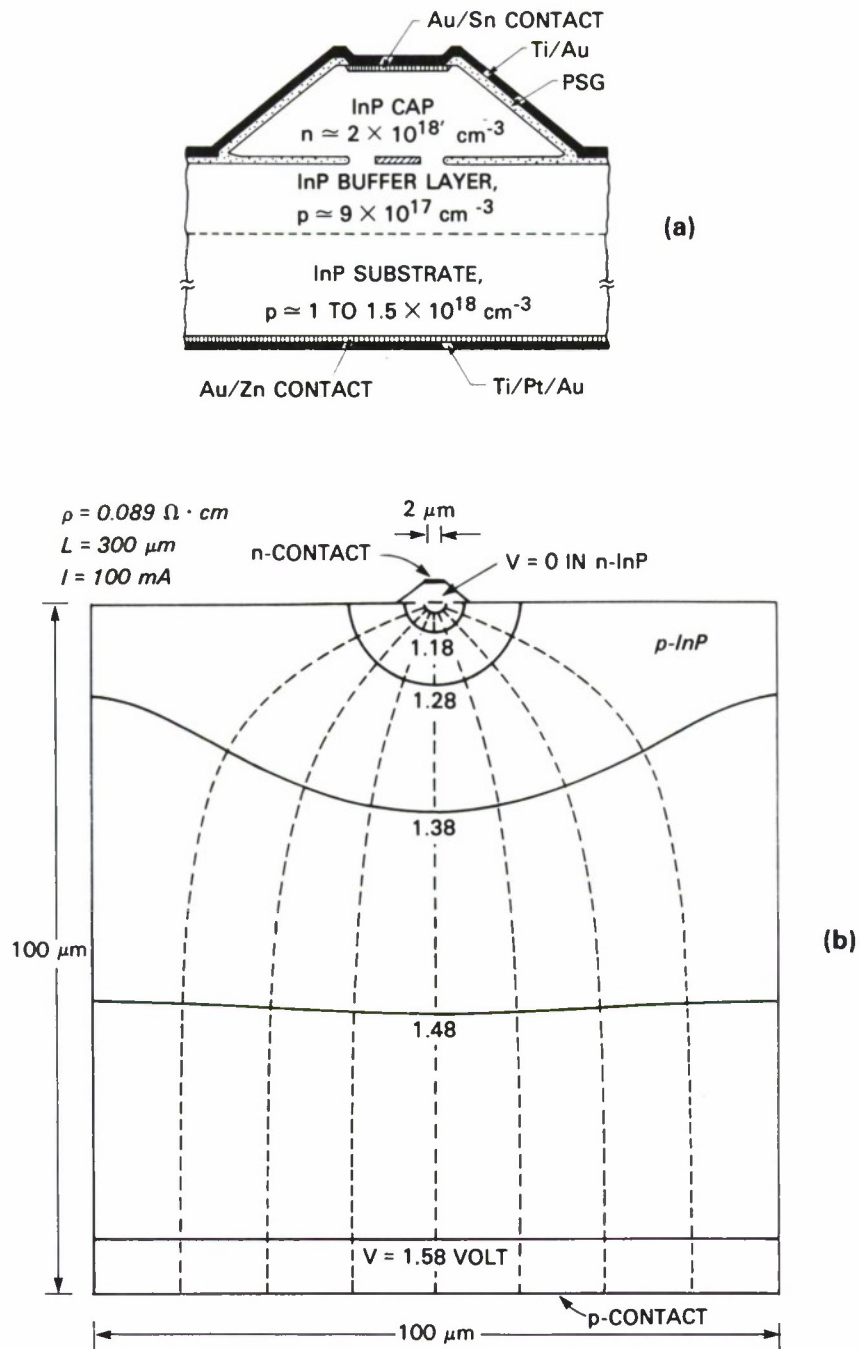


Figure 1-4. (a) Transverse cross-sectional view of a p-substrate mass-transported GaInAsP/InP BH laser. (b) Calculated current and voltage distributions in substrate.



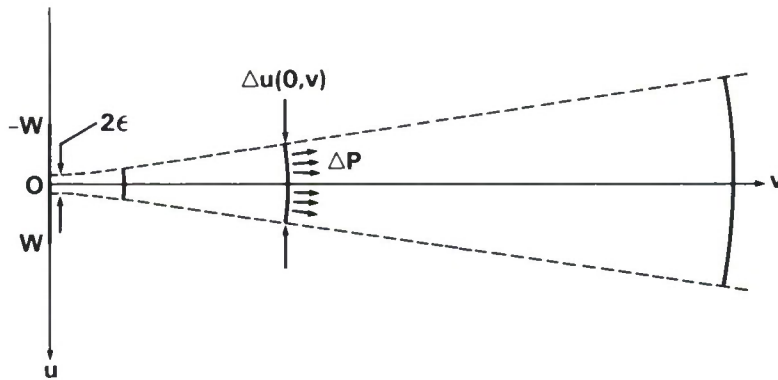


Figure 1-5. Thin stream of heat flow used in calculation of temperature  $T(v,0)$  along  $v$ -axis (cf. Figure 1-4). Line segment from  $u = -W$  to  $u = W$  represents laser active region.

where  $\Delta I \equiv J(0,0)2\epsilon L$  is the electrical current flowing in the region, with  $J(0,0)$  being the current density at the origin. By using the definition of  $\Phi$  it can easily be shown that

$$J(0,0) = \frac{I}{\pi L} \frac{\partial \Phi}{\partial v}(0,0)$$

and

$$V(0,v) - V(0,0) = \frac{\rho I}{\pi L} \Phi(0,v) .$$

Therefore Equation (1-2) can be written as

$$\Delta P = \frac{2\epsilon}{\pi^2 L} \rho I^2 \Phi(0,v) \frac{\partial \Phi}{\partial v}(0,0) . \quad (1-2a)$$

At  $v = v$ , the power  $\Delta P$  flows through the cross-sectional area  $\Delta A \equiv \Delta u(0,v)L$  via a temperature gradient  $\frac{\partial T}{\partial v}(0,v)$  and is described by the heat-conduction equation

$$-K \frac{\partial T}{\partial v} = \frac{\Delta P}{\Delta A} \quad (1-3)$$

where  $K$  is the thermal conductivity of InP. By using Equation (1-2a) for  $\Delta P$  and Equation (1-1) for  $\Delta u(0,v)$ , we have

$$-K \frac{\partial T}{\partial v}(0,v) = \frac{\rho I^2}{\pi^2 L^2} \Phi(0,v) \frac{\partial \Phi}{\partial v}(0,v) . \quad (1-3a)$$

Then, integration along the  $v$ -axis yields

$$T(0,0) - T(0,v) = \frac{\rho I^2}{2\pi^2 K L^2} [\Phi(0,v)]^2 \quad (1-4)$$

with  $\Phi(0,v) = \sinh^{-1}[\sinh(\pi v/2s)/\sin(\pi W/2s)]$  as obtained previously,<sup>2</sup> where  $2s$  is the sidewall spacing,  $2W$  is the active region width, and  $v$  is the substrate thickness. Equation (1-4) permits a direct calculation of the temperature profile.

It should be noted that Equation (1-4) is true also for  $u \neq 0$ . This can be seen readily by verifying that

$$T(u,v) \equiv T(0,0) - \frac{\rho I^2}{2\pi^2 K L^2} [\Phi(u,v)]^2 \quad (1-4a)$$

satisfies the two-dimensional heat-conduction equation

$$-K\nabla^2 T(u,v) = [\nabla V(u,v)]^2 / \rho \quad (1-5)$$

(Note that the right-hand side of Equation (1-5) is the product of the electric field ( $\mathbf{E} \equiv -\nabla V$ ) and the current density ( $\mathbf{J} \equiv -\nabla V / \rho$ ), and is the ohmic heat generated per unit time per unit volume.) The verification can be done easily by using the differentiation formulas and  $\nabla^2 \Phi = 0$  to show that  $\nabla^2 \Phi^2 = 2(\nabla \Phi)^2$ .

By using the previously obtained substrate spreading resistance,  $R = \rho \Phi(0,v) / \pi L$ , Equation (1-4) can be written as

$$\Delta T = R I^2 R_T / 2 \quad (1-4b)$$

where  $\Delta T \equiv T(0,0) - T(0,v)$  is the temperature rise at the active region (vs the heatsink) and  $R_T \equiv \Phi(0,v) / \pi K L$  is the thermal resistance for heat generated at the active region, as obtained previously. Since  $R I^2$  is the total ohmic heat generated per unit time by the entire substrate,  $R_T / 2$  can be interpreted as the thermal resistance for the ohmic heating in the substrate, which is exactly half the thermal resistance for heat generated in the active region.

The solid curves in Figure 1-6 show calculated ohmic heating as a function of operating current for  $p = 1.5 \times 10^{18} \text{ cm}^{-3}$ ,  $\mu_p = 75 \text{ cm}^2/\text{V s}$  and four different device lengths. The temperature rise shows a quadratic dependence on the current which is characteristic of ohmic heating. There is also a strong (inverse quadratic) dependence on the device length, because the electrical and thermal resistances are both inversely proportional to the device length. Note that the temperature rise stays below  $5^\circ\text{C}$  for devices longer than  $250 \mu\text{m}$  operated below  $150 \text{ mA}$ .

Although the present analysis has been made for the mass-transported BH lasers, it is expected to serve as a good approximation for other types of p-substrate BH lasers also. This is because the differences in the device geometry occur near the active region which is much smaller than the substrate.

Z. L. Liao  
J. N. Walpole

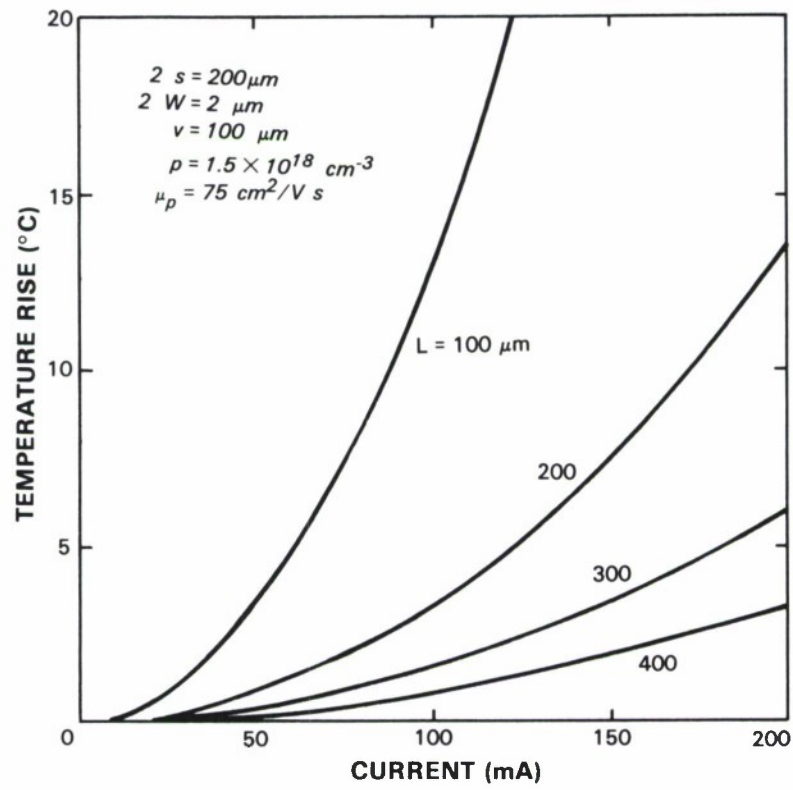


Figure 1-6. Calculated temperature rise of active region due to ohmic heating in p-type substrate when device is mounted junction-side up on heatsink.

### 1.3 PROTON IRRADIATION AND ANNEALING OF Fe-DOPED SEMI-INSULATING InP

For optimally chosen doses, proton bombardment of p-type InP can result in high-resistivity surface layers; however, only moderate increases in the resistivity of n-type material<sup>3,4</sup> are possible. For high proton doses, the resistivity of both p- and n-type material approaches the same value, about  $10^3 \Omega\text{-cm}$  (n-type). This type conversion is attributed generally to radiation-induced defects which act to pin the Fermi level at about 0.3 eV below the InP conduction band edge.<sup>3</sup> For many device applications, change in the resistivity of the semi-insulating InP substrate due to damage effects is also important. Bulk semi-insulating InP is usually grown by adding Fe, a deep acceptor with an energy level located near the center of the band gap,<sup>5</sup> to the melt during crystal growth. In this report we present results on radiation-induced resistivity variations of Fe-doped semi-insulating InP as a function of proton dose and bulk Fe concentration. The annealing behavior of high-dose-induced defects is examined also.

Fe-doped InP crystals with Fe concentrations ranging from  $9 \times 10^{15}$  to  $2 \times 10^{17} \text{ cm}^{-3}$  were investigated in these experiments. Samples from each crystal were bombarded with 100-keV  $\text{H}^+$  up to a total accumulated dose of  $4.4 \times 10^{15} \text{ cm}^{-2}$ . Hall measurements using the Van der Pauw technique were performed after each bombardment to determine the sheet resistivity, carrier concentration, and mobility. In addition, several samples were annealed at temperatures up to  $750^\circ\text{C}$  in order to determine the temperature stability of the defects produced by the proton bombardment.

The InP:Fe sample with an Fe concentration of  $9 \times 10^{15} \text{ cm}^{-3}$  was not semi-insulating prior to bombardment and had a bulk resistivity and electron concentration of about  $0.65 \Omega\text{-cm}$  and  $1.3 \times 10^{16} \text{ cm}^{-3}$ , respectively. Samples with Fe concentrations  $3 \times 10^{16} \text{ cm}^{-3}$  and above were semi-insulating prior to bombardment and, as shown in Figure 1-7, did not begin to exhibit measured sheet conduction until they had received an accumulated proton dose  $\geq 3 \times 10^{13} \text{ cm}^{-2}$ . The average resistivity  $\rho$  in the bombarded layer was obtained from the sheet resistivity  $\rho_s$  by assuming that the damaged layer for 100-keV  $\text{H}^+$  in InP is  $1.0\text{-}\mu\text{m}$  thick. Between proton doses of  $4.4 \times 10^{13}$  and  $4.4 \times 10^{14} \text{ cm}^{-2}$ , the resistivity in all samples varied by less than an order of magnitude, and in general exhibited a broad local minimum. The minimum was more pronounced in crystals with the lower Fe concentrations. For doses above  $4.4 \times 10^{14} \text{ cm}^{-2}$ , the sheet resistivity on all samples again decreased rapidly with increasing dose. For accumulated doses of less than  $1 \times 10^{14} \text{ cm}^{-2}$ , our measurements are in reasonable agreement with those of Thompson *et al.*<sup>4</sup> and Yuba *et al.*<sup>6</sup> No previous work, however, has been reported at the higher-dose levels.

From our results, it appears that below about  $4 \times 10^{13} \text{ H}^+/\text{cm}^2$ , the electrical characteristics of the bombarded layers are still dominated by the deep acceptor Fe levels. Above  $4 \times 10^{13} \text{ H}^+/\text{cm}^2$ , they become dominated by the defects produced by the proton bombardment. The resistivity is fairly constant for doses between  $4 \times 10^{13}$  and  $4 \times 10^{14} \text{ cm}^{-2}$ . This is most likely because of the pinning of the Fermi level in the upper half of the band gap,  $\approx 0.25 \text{ eV}$  from the conduction band, by defect levels produced by the bombardment. Yuba *et al.*<sup>6</sup> have identified a defect level at 0.19 eV below the conduction band. To pin the Fermi level over a range of damage,



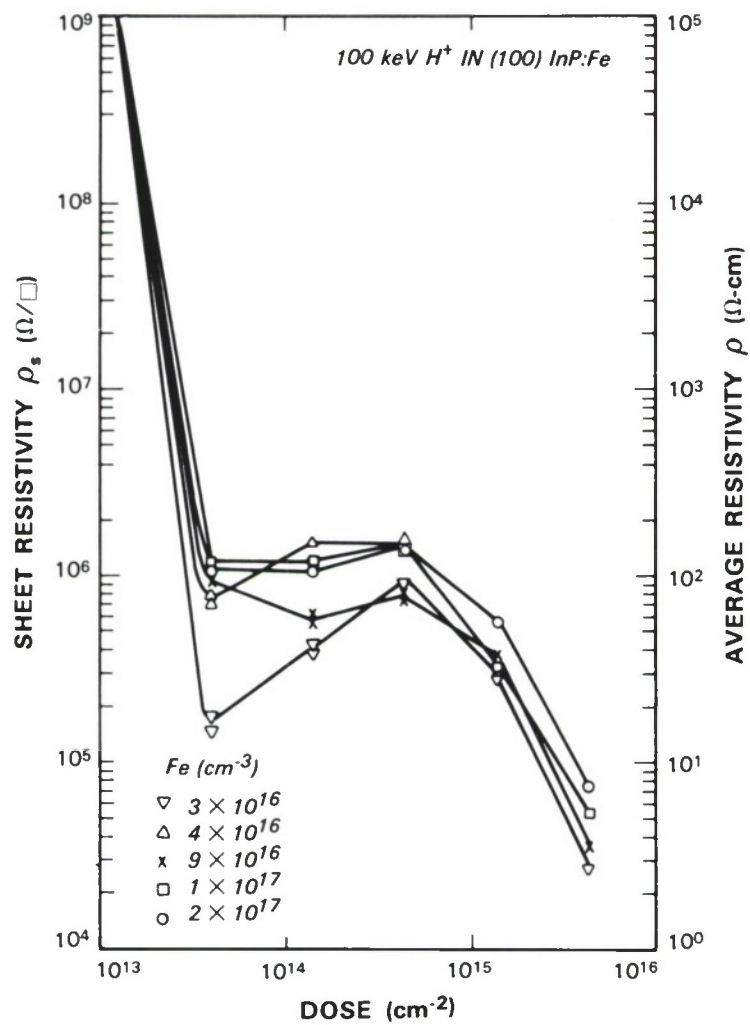


Figure 1-7. Resistivity vs accumulated dose for several InP:Fe crystals irradiated with 100-keV protons.

however, requires the production of both donor and acceptor levels. The necessity of having both donors and acceptors can also be deduced from the fact that proton bombardment pins the Fermi level on both n- and p-type starting material at about the same point<sup>3</sup> as in the Fe-doped crystals. In the dose range of fairly constant resistivity, increases in resistivity occur because of a decrease in electron mobility and a small decrease in carrier concentration. This decrease is due to either an increase in the net production of acceptor levels to donor levels or the production of a new acceptor level with increasing dose. For doses greater than  $4 \times 10^{14} \text{ cm}^{-2}$ , hopping conduction through the deep levels could be responsible for the decrease in resistivity with dose. It may be possible to verify this by measuring the frequency dependence of the resistivity in this dose range.

To gain further insight into the defect production mechanism under high-dose proton irradiation, annealing studies were performed on several Fe-doped InP wafers implanted with  $3 \times 10^{14}$ - and  $3 \times 10^{15}$ - $\text{cm}^{-2}$  100-keV protons. Samples cut from these wafers were annealed up to temperatures of  $750^\circ\text{C}$ , with or without phosphosilicate glass (PSG) encapsulation, for 30 min in flowing  $\text{N}_2$ . As shown in Figure 1-8, the resistivity of high-dose proton-irradiated samples annealed at  $250^\circ\text{C}$  decreases by two orders of magnitude compared with that of the unannealed irradiated sample. This effect is much more drastic than the slight decrease of sheet resistivity reported for  $1 \times 10^{14}$ - $\text{cm}^{-2}$  proton irradiation under similar anneal conditions.<sup>6</sup> As determined from the Hall measurements, this observed decrease in resistivity is due primarily to an increase in electron conduction, which indicates that the deep acceptors produced by the proton irradiation may anneal out faster than the deep donors. For anneal temperatures  $>250^\circ\text{C}$ , the sheet resistivity increases monotonically with temperature until  $450^\circ\text{C}$ , where the Fe-doped bombarded layer is again semi-insulating. When a PSG encapsulant is used during the anneal, the samples remain semi-insulating up to  $750^\circ\text{C}$ , the highest anneal temperature used. This confirms that the degradation in resistivity observed by Yuba *et al.*<sup>6</sup> for anneals  $>400^\circ\text{C}$  is due to the loss of P. The increase in resistivity observed between  $250^\circ$  and  $450^\circ\text{C}$  in these high-dose bombarded layers corresponds to the removal of the 0.19-eV level observed by Yuba *et al.*<sup>6</sup> on low-dose bombarded samples at similar anneal temperatures.

J.D. Woodhouse  
J.P. Donnelly  
G.W. Iseler

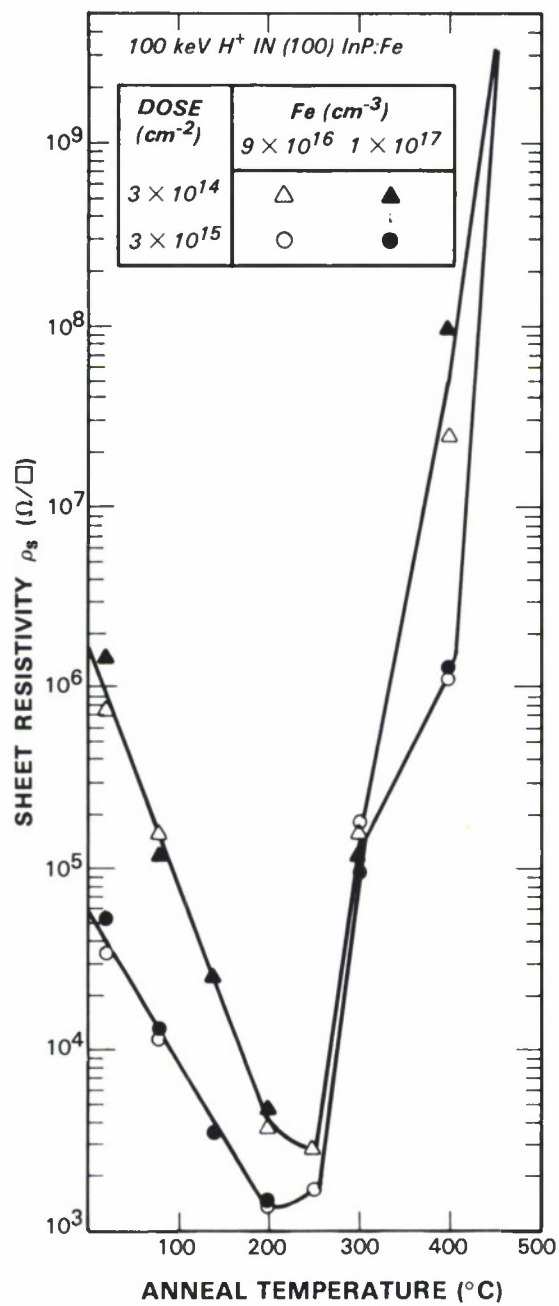


Figure 1-8. Resistivity vs anneal temperature for InP:Fe samples irradiated with  $3 \times 10^{14}$ - and  $3 \times 10^{15}$ - $cm^{-2}$  100-keV protons.

## 1.4 16-Gb/s LARGE-SIGNAL DIGITAL MODULATION OF DIODE LASERS

The modulation of diode lasers under nonsinusoidal large-signal conditions cannot be inferred from the small-signal characteristics. Calculations by Tucker<sup>7</sup> suggest that lasers can operate at data rates equal to their bandwidth; however, the analysis did not include arbitrary bit sequences. Previous large-signal modulation experiments have been performed with external modulation at 8 Gb/s (Reference 8), direct modulation at 8 Gb/s (Reference 9), and near-sinusoidal drive at 16 Gb/s (Reference 10). We report here large-signal modulation of p-type substrate 1.3- $\mu\text{m}$  GaInAsP diode lasers at a rate of 16 Gb/s with several different bit sequences.

A special digital word generator shown in Figure 1-9 was constructed to produce a limited set of 16-Gb/s word sequences. The generator is driven by a 2-GHz frequency-synthesized source and a 2-W TWT amplifier, protected with a microwave isolator. The signal from the isolator is split into four lines, each with a separate 2-GHz comb generator and a different amount of delay. The delay lines are staggered by 125 ps (two bit spacings at 16 Gb/s) in order to produce four equally spaced pulses when recombined. Before recombining the four pulses, the dc component of each comb generator is removed and the pulses are routed through microwave switches which can introduce an additional delay of 62.5 ps (one bit spacing at 16 Gb/s). The pulses are combined in a broadband 2- to 18-GHz combiner. The switches allow different word patterns to be

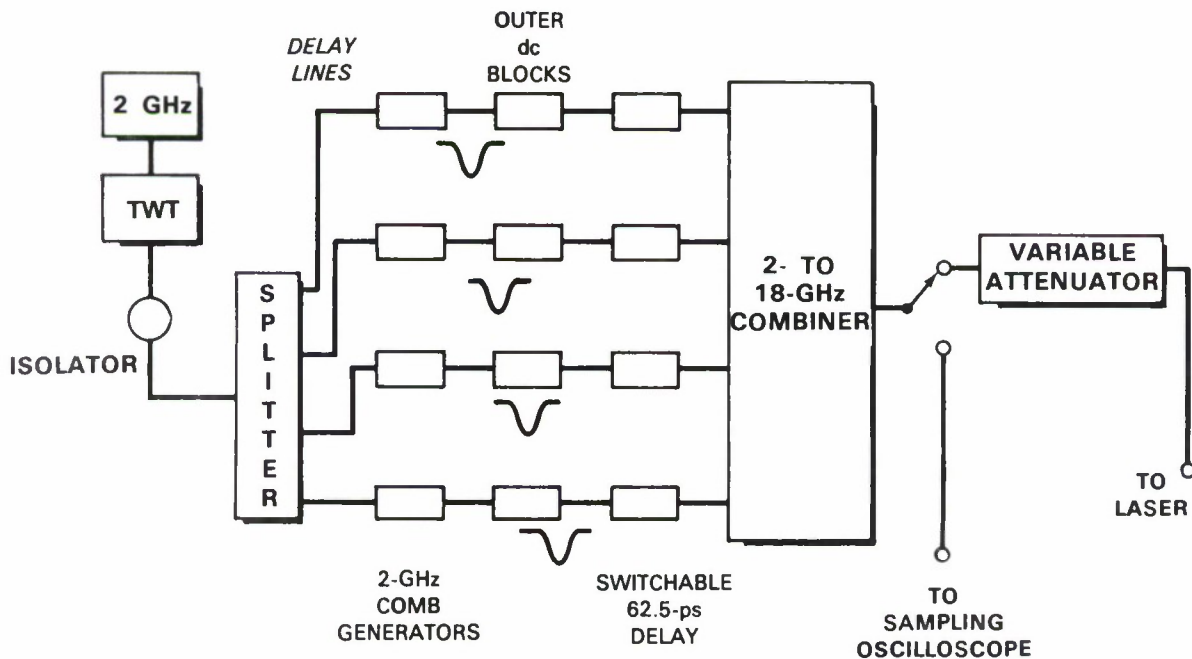


Figure 1-9. Schematic of 16-Gb/s digital word generator. Words are synthesized by combining appropriately delayed pulses from four comb generators.



generated, but since the pulse sequence repeats every 500 ps, only four unique word patterns can be generated. The level of the output can be adjusted by variable attenuators in steps of 1 dB over a range of 0 to 99 dB. The output can also be switched to a sampling oscilloscope to record the electrical drive to the laser. Compared with previous word generators<sup>8-10</sup> based on one or two comb generators, that shown in Figure 1-9 is capable of higher output levels and a wider variety of word patterns.

The word generator was connected to the laser through a 0.1- to 18-GHz bias network and a short length of cable. The dc bias current of the laser was set at 80 mA, at which bias the small-signal -3-dB modulation frequency of the laser was 16 GHz (Reference 11). The laser output was detected by a 22-GHz PIN detector<sup>†</sup> and an 18-GHz sampling oscilloscope. The laser response to three of the four possible word patterns is shown in the upper part of the oscilloscope photographs in Figure 1-10. The electrical drive traces shown in the lower part of the photographs have been aligned with the detected laser output to compensate for the difference in delay between the optical and electrical paths. For the 11001100 sequence seen in Figure 1-10(a), the laser reproduces the electrical drive reasonably well. The 10101100 sequence is reproduced reasonably well also, as shown in Figure 1-10(b). The 00101101 sequence shown in Figure 1-10(c) shows a slight amount of degradation in the 00 portion of the sequence. The low level is somewhat rounded and suggests some pattern dependence for 00 preceded by 01, as shown in Figure 1-10(c), compared with 00 preceded by 11, as shown in Figures 1-10(a) and (b). The fourth distinct word pattern, a series of equally spaced pulses, is not shown but is reproduced faithfully by the laser.

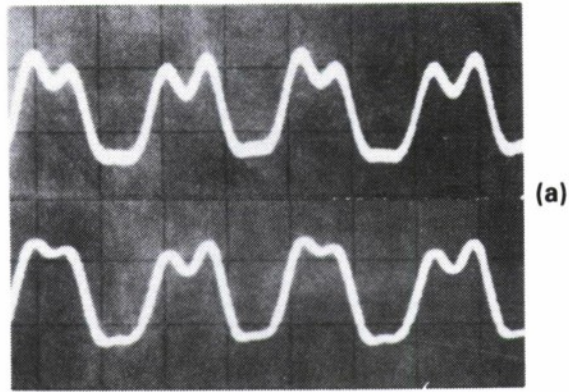
The results shown in Figure 1-10 were obtained with a calculated peak ac-electrical-drive current to the laser of 35 mA. Decreasing the electrical-drive current decreased the amplitude of the detected signal but did not alter markedly the shape of the waveform. In all cases, the laser followed the electrical drive with only a slight amount of pattern dependence. These p-type-substrate mass-transported lasers can transmit high-quality digital optical signals at rates of 16 Gb/s and should prove useful for future high-speed systems.

D.Z. Tsang  
Z.L. Liao

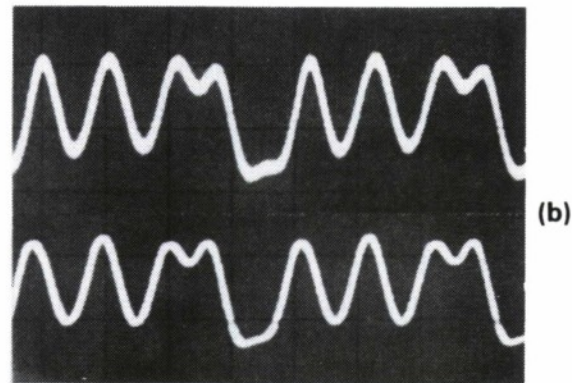
---

<sup>†</sup> We would like to thank C.A. Burrus and J.E. Bowers of AT&T Bell Laboratories for the detector used in this study.

11001100



10101100



00101101

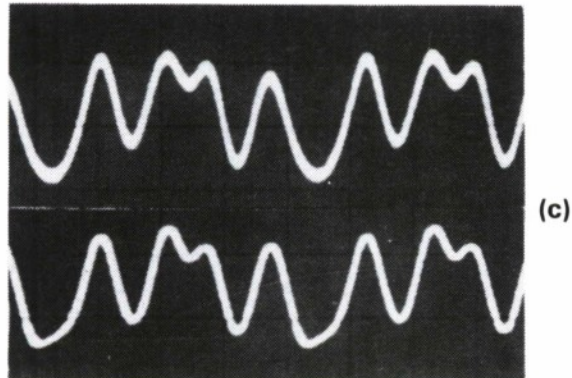


*Figure 1-10. 16-Gb/s digital modulation of a laser biased for a -3-dB frequency of 16 GHz. Top trace corresponds to detected signal. Bottom trace corresponds to electrical drive. Time scale is 100 ps/div.*

## REFERENCES

1. R.H. Rediker, R.P. Schloss, and L.J. Van Ruyven, *Appl. Phys. Lett.* **46**, 135 (1985).
2. Solid State Research Report, Lincoln Laboratory, MIT (1985:4), p. 6, DTIC AD A-172872.
3. J.P. Donnelly and C.E. Hurwitz, *Solid-State Electron.* **20**, 727 (1977), DDC AD-A 054406.
4. P.E. Thompson, S.C. Binari, and H.B. Dietrich, *Solid-State Electron.* **26**, 805 (1983).
5. G.W. Iseler, *Institute of Physics Conf. Ser. No. 45*, 1979, p.144.
6. Y. Yuba, Y. Judai, K. Gamo, and S. Namba, *Physica B & C* **116**, 461 (1983).
7. R.S. Tucker, *Electron. Lett.* **20**, 802 (1984).
8. R.C. Alferness, S.K. Korotky, C.H. Joyner, and L.L. Buhl, in *Tech. Digest 4th Int. Conf. on Integrated Optics and Opt. Fiber Commun.* (Tokyo), June 1983, pp. 242-243.
9. K.Y. Lau and A. Yariv, *Appl. Phys. Lett.* **47**, 84 (1985).
10. C. Lin and J.E. Bowers, *Electron. Lett.* **21**, 906 (1985).
11. Solid State Research Report, Lincoln Laboratory, MIT (1986:4), p. 6.

## 2. QUANTUM ELECTRONICS

### 2.1 STUDIES OF TRANSIENT EFFECTS IN Ti:Al<sub>2</sub>O<sub>3</sub> LASER TUNING

The previously described<sup>1</sup> electro-optically tuned Ti:Al<sub>2</sub>O<sub>3</sub> laser has been investigated further. The current version of the cavity is shown schematically in Figure 2-1. The tuning voltage is applied across the thickness of the LiNbO<sub>3</sub> crystal, in a direction perpendicular to the plane of the figure. Because of the prisms' dispersive action, the output beam translates slightly as the laser is tuned; transient tuning phenomena then can be investigated simply by directing the laser beam onto a position-sensitive photodetector. Initial experiments have been performed with just a single-element lateral-effect photodiode.<sup>2</sup> Figure 2-2(a) shows the tuning response to a triangular-wave driving voltage when only the LiNbO<sub>3</sub> crystal, operated in its lowest tuning order (one wave retardation), is present in arm "a" of the cavity. Tuning occurs in discrete jumps of approximately 4.8 nm. This behavior, initially not understood, has been shown to be related to the birefringence of the laser crystal. Ideally, the optic axis should be perpendicular to the laser beam direction of propagation and in the plane of polarization determined by the Brewster-cut prism and crystal faces (Figure 2-1). Even a small tilt of the optic axis out of this plane, however, will generate an appreciable modulation transmission through the crystal as the latter will behave as a retardation plate between polarizers. The preferred lasing wavelengths will be determined by the condition that the single-pass retardation through the laser crystal be an integer number  $M_c$  of wavelengths

$$\Delta n L_c = M_c \lambda$$

where  $\Delta n$  is the Ti:Al<sub>2</sub>O<sub>3</sub> birefringence and  $L_c$  the crystal length. The above condition corresponds to wavelength steps  $\Delta \lambda = \lambda^2 / L_c \Delta n$ , in precise agreement with the data of Figure 2-2(a).

To achieve the required stepless tuning, better tuner selectivity is needed corresponding to operation of the tuner crystal on a higher retardation order. This can be achieved by using higher voltages or by "biasing" the LiNbO<sub>3</sub> crystal with a cascaded, naturally birefringent plate, making a 45° angle with the plane of the figure. If  $\Phi_e = \delta n L$  is the electro-optic retardation in the LiNbO<sub>3</sub> crystal and  $\Phi_b = \Delta n T$  the bias retardation in the sapphire plate (for one pass), the lasing wavelength selected by the tuner is

$$\lambda = (2\Phi_e + 2\Phi_b) / M$$

where  $M$  is the total retardation order. The relative bandwidth of each tuning order,  $\Delta \lambda / \lambda$ , is proportional to  $1/M$ ; a sufficiently thick bias plate, therefore, should allow continuous tuning. This is shown in Figure 2-2(b), where a 1-mm-thick sapphire plate was used. The residual steps in the tuning transient are probably related to the sapphire bias plate acting as an etalon.

Current work is aimed at determining the minimum tuner retardation that will be required for single cavity mode selection, as well as the number of tuner stages necessary for continuous tuning through the Ti:Al<sub>2</sub>O<sub>3</sub> gain bandwidth.

V. Daneu



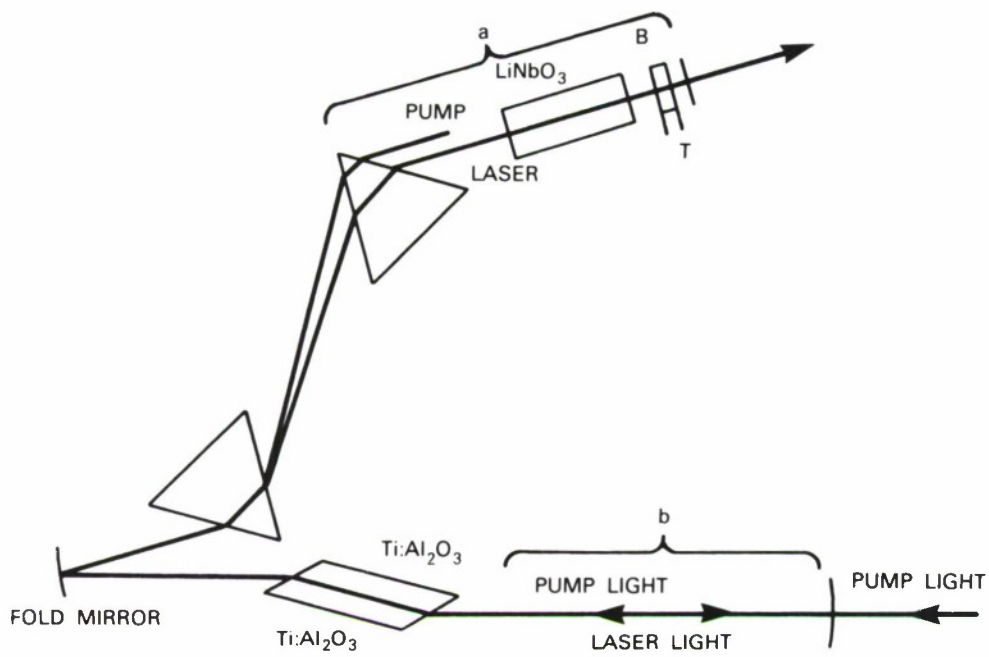
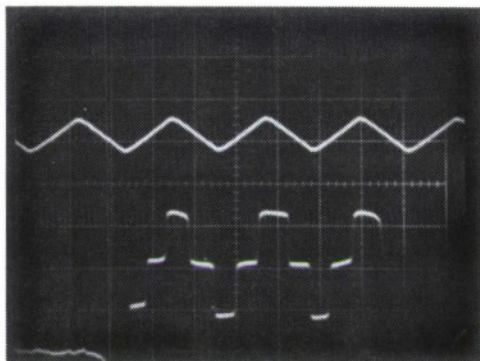


Figure 2-1. Cavity layout of electro-optically tuned  $\text{Ti:Al}_2\text{O}_3$  laser.

DRIVE  
VOLTAGE  
50 V/div

WAVELENGTH  
4 nm/div

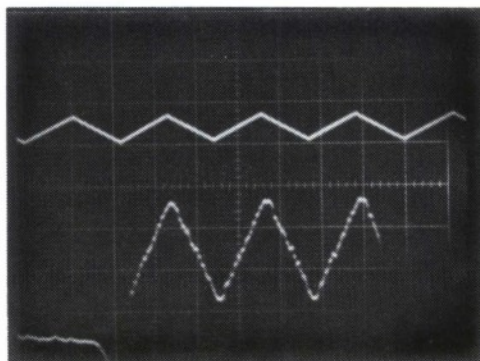


(a)  
TUNER  
RETARDATION:  
1  $\lambda$

200  $\mu$ s/div

DRIVE  
VOLTAGE  
500 V/div

WAVELENGTH  
4 nm/div



(b)  
TUNER  
RETARDATION:  
12  $\lambda$

Figure 2-2. Tuning response to a triangular-wave drive voltage: (a) only  $\text{LiNbO}_3$  crystal in cavity; (b)  $\text{LiNbO}_3$  crystal and optical bias plate in cavity.

## 2.2 ACOUSTO-OPTIC MODULATOR AS A UNIDIRECTIONAL DEVICE IN A RING LASER

The acousto-optic modulator has been used to force unidirectional operation of a ring dye laser and a ring  $\text{Ti:Al}_2\text{O}_3$  laser. Three different acousto-optic modulators have been used: an antireflection-coated barium-titanate traveling-wave modulator (AOM1), a Brewster-angle quartz traveling-wave modulator (AOM2), and a Brewster-angle quartz standing-wave modulator (AOM3). For AOM1, the acousto-optic diffraction is in the plane of the ring; for AOM2 and AOM3, diffraction is perpendicular to the plane of the ring. AOM1 was used in a dye laser; AOM2 and AOM3 were used in the  $\text{Ti:Al}_2\text{O}_3$  laser. Unidirectional operation has been achieved using RF modulation frequencies between 12 and 125 MHz. For AOM2, very low insertion loss was observed with a laser threshold increase of only 5 percent. One of the ring-laser cavity configurations is shown in Figure 2-3.

Unidirectional operation is obtained as follows: The acousto-optic crystal is placed in the ring cavity and the laser realigned to achieve lasing. After RF power is applied, typically  $<3$  W, the acousto-optic modulator angle is adjusted to produce unidirectional operation. The most efficient and stable operation of the laser is achieved when the acousto-optic modulator is placed near the Bragg angle. Adjustment of the intracavity elements can be used to cause the laser to switch lasing direction. Specifically, the lasing direction can be switched electronically by changing the frequency applied to the acousto-optic modulator. The acousto-optic modulator has been used as a unidirectional device (1) in a laser with very little wavelength selectivity (only the output mirror), (2) in a single-frequency laser, and (3) in a mode-locked laser.

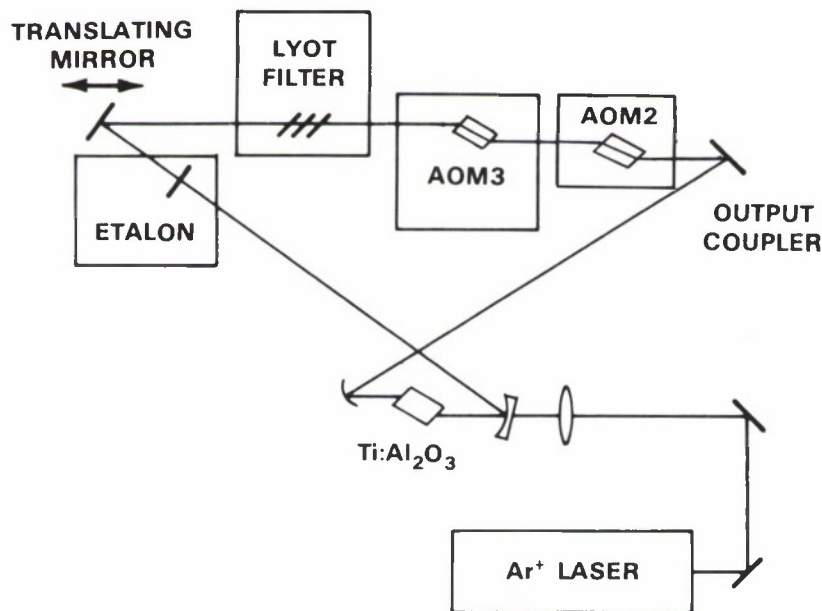


Figure 2-3. Cavity used for obtaining single-frequency and mode-locked operation of a unidirectional ring  $\text{Ti:Al}_2\text{O}_3$  laser. Single-frequency operation is obtained with no voltage applied to AOM3 and 12 to 50 MHz applied to AOM2. Mode-locked operation is obtained by applying 120 MHz to AOM3 in addition.

One parameter that provides a quantitative measure of unidirectionality is the intensity ratio for the two counterpropagating laser directions. When the acousto-optic modulator is used in a  $\text{Ti:Al}_2\text{O}_3$  laser with no optical elements in the laser cavity, a ratio of 2000:1 is observed. This ratio is better than that typically achieved with an external retroreflector.<sup>3</sup>

The interaction that causes a gain difference in the two directions requires at least one, and probably many, round-trips through the ring. The experiment involves blocking the diffracted beam from the acousto-optic modulator and observing a transition from unidirectional to bidirectional lasing in the ring. The blocking of the diffracted beam is accomplished by gradually lowering a knife edge toward the laser beam. The location of the unidirectional to bidirectional transition can be determined within 0.1 mm, and the position of this transition is independent of the direction of the traveling wave in the unidirectional ring laser. This experiment was carried out for several locations of the knife edge in the laser cavity and indicates that the diffracted beam must travel more than once around the laser cavity.

When the ring laser is operated unidirectionally under low RF driving power into the modulator, the diffracted radiation does not necessarily show up in the output beam and there is no observed increase in the laser threshold. If the applied RF power is increased sufficiently, the laser threshold rises and a diffraction peak can be observed on one side of the laser beam, as shown in Figure 2-4. The diffraction peak is not the sharp single peak observed from an external acousto-optic modulator. The diffuse peak probably consists of the overlap of many beams arising from multiple passes through the ring cavity. Indeed, careful observations show an interference pattern (spacings of  $\sim 2$  mm) in the diffracted beam arising from multiple passes of the first-order diffraction peak. It is important to note that different orders of AOM2 cannot cause a stationary interference pattern because each order is at a different frequency. For instance, an interference pattern between the laser beam and the first-order diffraction peak would be washed out in a time period of 50 ns for an acoustic frequency of 20 MHz.

Calculations of the optical path of the first-order diffracted beam in the ring-laser cavity show that it does not traverse the same path in each round-trip. The location of the diffracted beam after each round-trip is bounded by an amount directly related to the Bragg diffraction angle and scales linearly with acoustic frequency. Although quantitative agreement between the observed and calculated laser beam profiles is not obtained, a linear relationship is observed between the acoustic frequency and the distance of the diffracted beam from the laser beam.

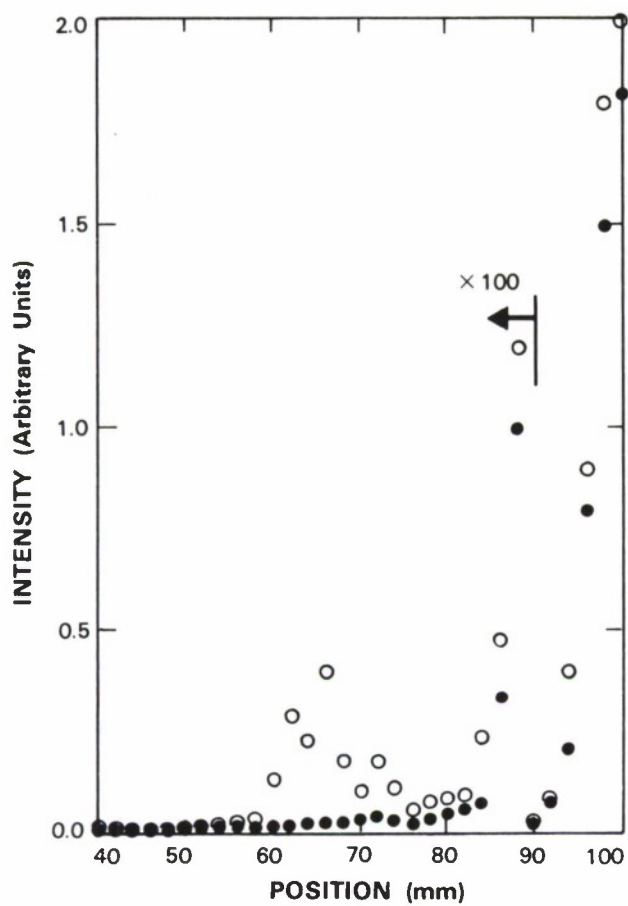
In conclusion, an acousto-optic modulator causes unidirectional lasing in a ring cavity. The modulator has very low insertion loss, allows electronic switching of laser direction, and does not couple the two directions in the ring. The acousto-optic modulator has been used in unidirectional ring lasers for both frequency and mode-locked operation. The unidirectional output is caused by a gain difference in the two ring directions arising from multiple passes of the diffracted beam through the ring-laser cavity. We believe an interference of the diffracted and laser beams in the gain medium can cause such a gain difference.

P. A. Schulz  
A. Walther  
R. Roy†

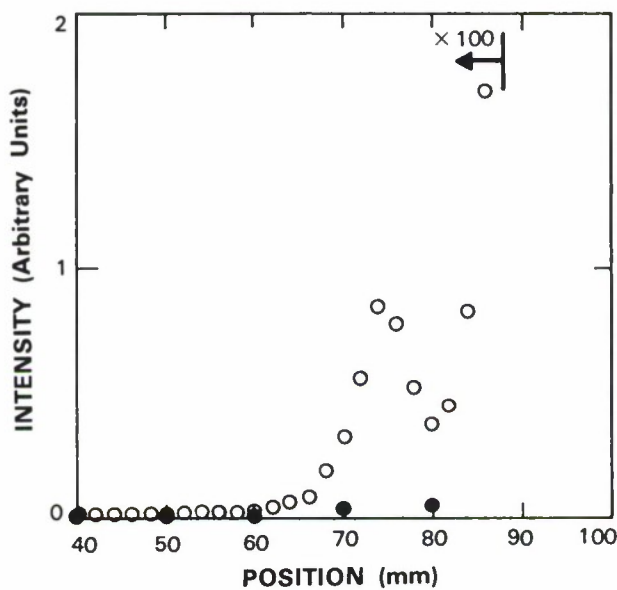
---

† Author not at Lincoln Laboratory.





(a)



(b)

Figure 2-4. Spatial profile of laser beam with and without an acousto-optic modulator for acoustic frequencies of (a) 22.8 and (b) 48.1 MHz. A first-order diffraction peak is observed in wings of laser beam.

### 2.3 MODE-LOCKED Ti:Al<sub>2</sub>O<sub>3</sub> LASER

Mode-locked operation of the Ti:Al<sub>2</sub>O<sub>3</sub> laser has been obtained. A Brewster-angle-cut Ti:Al<sub>2</sub>O<sub>3</sub> crystal is placed in a ring-laser cavity with a standing-wave acousto-optic modulator which acts as the mode-locker. The ring-laser cavity includes a Lyot filter and etalon for wavelength selection, and a second acousto-optic modulator to induce unidirectional laser operation (see Section 2.2). The free spectral range of the ring cavity is adjusted (by changing the length of the cavity) to 240 MHz; this free spectral range is selected because the mode-locker is designed to operate at 120 MHz. A standing acoustic wave is set up in the mode-locker so that twice during each cycle the standing-wave displacement is zero everywhere inside the crystal. When the displacement is zero, the mode-locker transmits all the incident light; at all other times the mode-locker diffracts part of the light, which quenches the laser. Consequently, very short light pulses are generated when the mode-locker frequency is exactly half the inverse of the round-trip transit time in the ring cavity<sup>4</sup> ( $\sim 4$  ns).

The 150-ps laser-pulse duration from the Ti:Al<sub>2</sub>O<sub>3</sub> mode-locked laser is observed using a detector with 50-ps risetime. The amount of RF power applied to the mode-locker affects the pulse duration. As little as 0.03 W causes mode-locked operation, with pulse durations of 700 ps. The shortest laser pulses are achieved with 4-W RF power, although in this case heating the crystal made mode-locked operation unstable. Stable operation with 300-ps pulses for 30 min could be achieved with 1.5-W RF power. These measurements were taken with no frequency-dispersive elements in the laser cavity.

With the etalon and Lyot filter in the ring cavity, the laser is single frequency with the mode-locker off. When RF power is applied to the mode locker, pulses are obtained with a duration of 500 ps. Under these conditions, the laser output is 70-mW average power and 500-mW peak power using 10-W CW argon-ion-laser pump power. As determined with a spectrum analyzer, there appear to be approximately 10 modes. This result implies that the product of the laser-pulse duration and the frequency spread is at the transform limit. A trade-off between number of laser modes and pulse duration was observed as the RF power to the mode-locker was varied, consistent with this conclusion.

P. A. Schulz  
D. J. Sullivan  
A. Sanchez

## 2.4 INJECTION-LOCKING A 1.32- $\mu\text{m}$ Nd:YAG LASER WITH A DIODE LASER

A Q-switched 1.32- $\mu\text{m}$  Nd:YAG laser has been injection-locked using the tunable output of a GaInAsP diode laser. Figure 2-5 shows a schematic of the Nd:YAG laser cavity and diode-laser injection-locking configuration. The 1.32- $\mu\text{m}$  GaInAsP diode laser<sup>5</sup> operated with a total output power of 3 mW on three longitudinal modes separated by 1 nm. Since the intermode spacing of the diode laser was greater than the 0.8-nm gain bandwidth of the 1.32- $\mu\text{m}$  Nd:YAG laser, only one mode of the diode laser fell within the gain region of the Nd:YAG laser. The Q-switched Nd:YAG laser operated with an average power of 1 W, pulse repetition rate of 1 kHz, and pulse width of 3  $\mu\text{s}$ . By either current or temperature tuning the wavelength of the diode laser, the wavelength of the Q-switched Nd:YAG laser could be tuned over a 0.1-nm range. Injection of the diode-laser radiation into the Nd:YAG laser cavity resulted in a reduction in the linewidth of the Nd:YAG laser from  $>8$  to 1 GHz, while the average power of the Nd:YAG laser remained the same. The spectral power of the Nd:YAG laser increased by a factor of 10.

The dependence of the injection-locking process on the intensity and polarization of the diode-laser radiation was investigated. It was found that diode-laser radiation, polarized either parallel or perpendicular to the direction of polarization of the Nd:YAG laser radiation, was capable of producing injection-locking. While the injection-locking process favored diode radiation polarized parallel to the Nd:YAG radiation, the arrangement of the apparatus allowed injection of much more diode radiation polarized perpendicular to the Nd:YAG radiation. Approximately 1- to 10-nW diode-laser radiation was found adequate for injection-locking the 1-W Nd:YAG laser. Previously,<sup>6</sup> we reported the Nd:YAG sum-frequency generation of sodium-resonance radiation. This generation requires the frequency control of a Nd:YAG laser operating at 1.3189  $\mu\text{m}$ . This control was accomplished by the angle tuning of an intracavity etalon. By injection-locking with a diode laser, better frequency and linewidth control of the 1.3189- $\mu\text{m}$  Nd:YAG laser may be possible.

T. H. Jeys  
D. K. Killinger  
A. A. Brailove

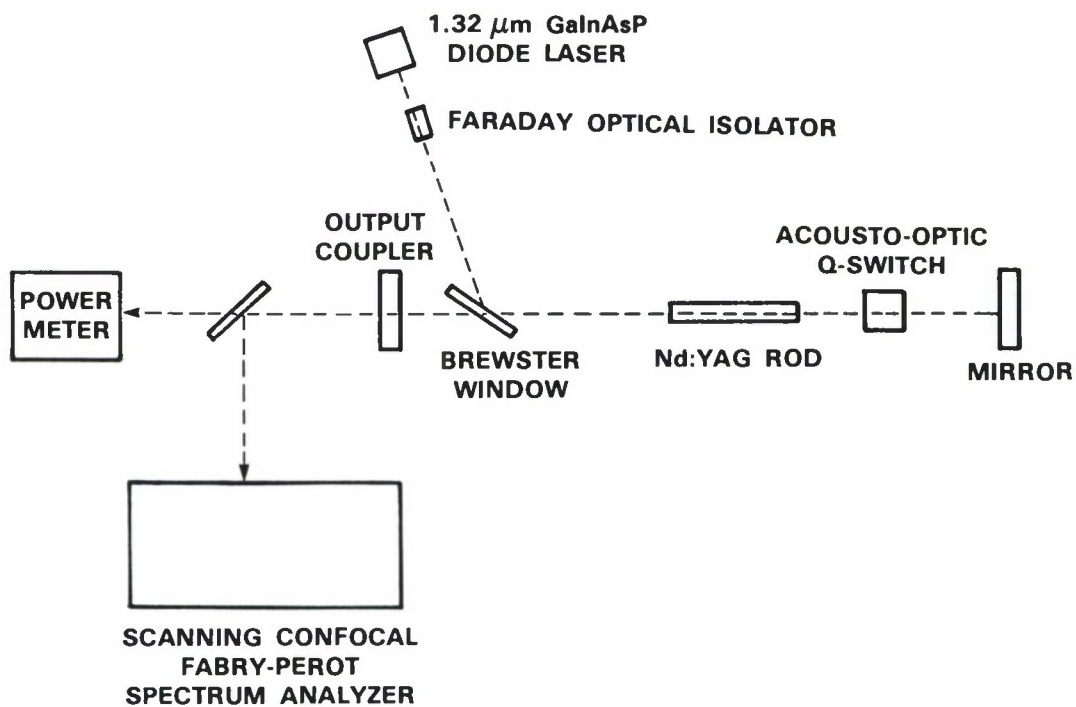


Figure 2-5. Injection-locking of a 1.32-μm Nd:YAG laser with a diode laser.



## 2.5 GENERATION OF SECOND HARMONIC OF Nd:YAG LASER RADIATION

The study of second-harmonic generation (SHG) from the 1064-nm output radiation of a long-pulse ( $\sim 100\text{-}\mu\text{s}$ ) Nd:YAG laser using KTP has continued and has been expanded to consider the use of  $\text{LiIO}_3$ . The laser output pulse consists of a packet of mode-locked pulses (100-ps FWHM) separated by 10 ns. (The mode-locked pulses provide the high peak power necessary for efficient SHG.) The laser pulse could be varied in duration from 50 to 200  $\mu\text{s}$ . In the following, the individual mode-locked pulses will be referred to as micropulses, while the packet of micropulses will be referred to as the macropulse. All of the SHG experiments described below used a macropulse length of  $\sim 100\text{ }\mu\text{s}$ . The temporal shape of the macropulse was not flat; a typical macropulse is shown in Figure 2-6. The power density values quoted below represent the average value of the individual micropulses, which is a factor of 100 greater than the average power density of the macropulse.

Previously,<sup>7</sup> we reported the achievement of  $\sim 40$ -percent conversion efficiency using a 7.3-mm KTP crystal, type II phase matching, and a macropulse rate of 1 Hz. With a more tightly focused incident beam, 50-percent efficiency was achieved at a power density of  $\sim 40\text{ MW}/\text{cm}^2$ . Surface damage was observed in this and other KTP crystals at input power densities ranging from 35 to slightly over 50  $\text{MW}/\text{cm}^2$ . Therefore, achievement of high-efficiency SHG using KTP crystals at their present stage of development appears marginal. This has led to an investigation of alternate materials.

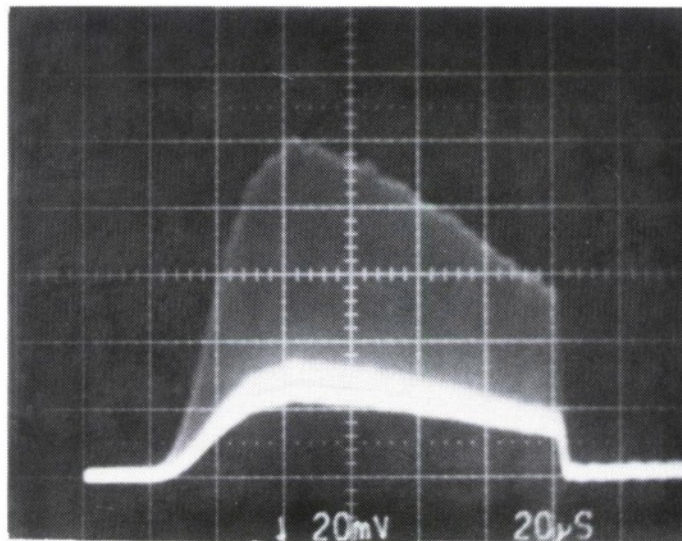


Figure 2-6. Temporal pulse shape of an  $\sim 100\text{-}\mu\text{s}$  macropulse (20 ns/div) from a Nd:YAG laser.

SHG experiments<sup>7</sup> using 1- $\mu$ s pulses from a Co:MgF<sub>2</sub> laser operating at 1650 nm showed that the damage threshold of LiIO<sub>3</sub> was significantly greater than that of KTP under the same conditions. This result indicated that efficient conversion of 1064 nm using LiIO<sub>3</sub> might be possible, an expectation borne out by our experiments. For the Nd:YAG laser described above, efficiencies >50 percent were achieved for LiIO<sub>3</sub> crystals 10, 15, and 25 mm in length. A plot of SHG efficiency vs input power density for the 25-mm crystal is shown in Figure 2-7. The input energy was 1 J/macropulse at a 1-Hz rate. Efficiencies >50 percent were achieved over a wide range of input power density. Up to  $\sim 25$  MW/cm<sup>2</sup>, the efficiency increases in a manner consistent with depletion effects. As the power density is increased beyond  $\sim 25$  MW/cm<sup>2</sup>, the efficiency falls below the theoretical depletion curve, presumably because of partial reconversion of the generated second harmonic back to the fundamental as a result of imperfect phase matching.

Thermal effects on SHG in LiIO<sub>3</sub> were investigated by operating the Nd:YAG laser at a constant 10-Hz rate, using a shutter to provide macropulses to the crystal at rates of 10, 5, 2.5, and 1.25 Hz. SHG efficiency vs input power density curves were measured at each of these rates. The results for 1.25 and 10 Hz are shown in Figure 2-8. Within the accuracy of our experiment, we see no effects of heating. This is due to the low optical absorption at 1064 and 532 nm, or the small value of  $\partial n/\partial T$ , the change of index of refraction with temperature, or both. An upper limit to the absorption was measured by means of a spectrophotometer and was found to be  $< 0.005$  cm<sup>-1</sup> at both 1064 and 532 nm. Nash *et al.*<sup>8</sup> reported that the phase-matching angle at 1084.5 nm changed by  $< 0.3^\circ$  from 20° to 256°C, indicating that  $\partial n/\partial T$  is extremely small. At the 10-Hz macropulse rate, an average power of  $> 5$  W was generated.

No damage occurred at the 1.25-, 2.5-, or 5-Hz macropulse rates up to an incident energy of  $\sim 170$  MW/cm<sup>2</sup>. LiIO<sub>3</sub> was found to damage at the 10-Hz macropulse rate. The damage occurred at the exit face of both an uncoated crystal and a crystal antireflection coated for 1064 nm.

In summary, LiIO<sub>3</sub> has been found to be a promising material for use in high-efficiency doubling of 100- $\mu$ s-long packets of mode-locked pulses from Nd:YAG lasers. High damage thresholds, as well as other properties of LiIO<sub>3</sub>, allow efficiencies of >50 percent to be achieved. Thermal effects appear to be negligible when operating at a 10-Hz macropulse rate, and average powers of more than 5 W of 532-nm radiation have been generated. The use of KTP to provide efficient frequency conversion of Nd:YAG radiation under conditions of a temporally long input pulse ( $\sim 100$   $\mu$ s) and high average power appears marginal at this time.

K. F. Wall  
N. Menyuk  
W. E. DeFeo

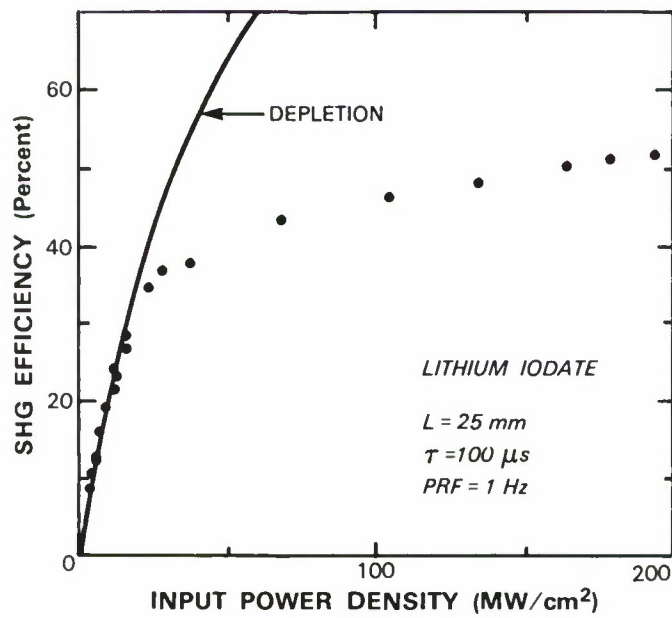


Figure 2-7. SHG efficiency vs incident power density from a Nd:YAG laser for a 25-mm-long  $\text{LiIO}_3$  crystal. Depletion curve is calculated based on initial slope of data.

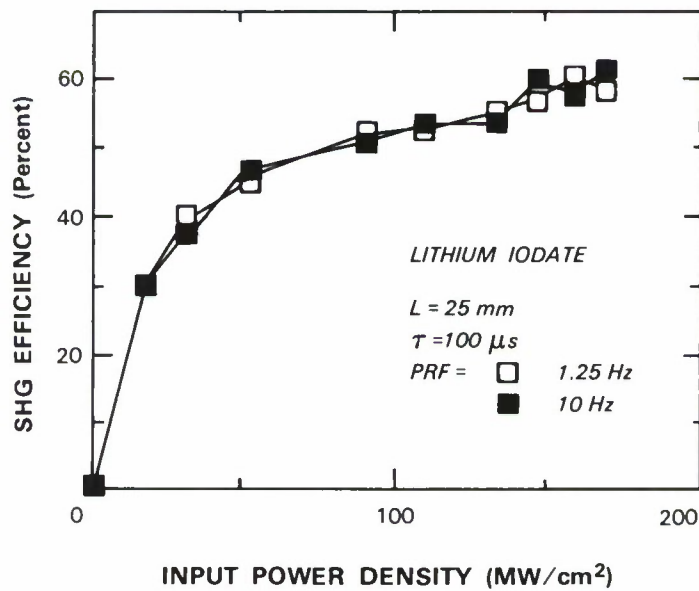


Figure 2-8. SHG efficiency vs incident power density curves for Nd:YAG macropulse rate of 1.25 and 10 Hz.

## REFERENCES

1. Solid State Research Report, Lincoln Laboratory, MIT (1986:3), p. 15.
2. W. Light, *Lasers and Appl.* **5**, No. 4, 75 (1986).
3. A.E. Siegman, *Lasers* (University Science Books, Mill Valley, 1986).
4. *Ibid.*
5. Z.L. Liao, J.N. Walpole, and D.Z. Tsang, *Appl. Phys. Lett.* **44**, 945 (1984).
6. Solid State Research Report, Lincoln Laboratory, MIT (1986:4). p. 16.
7. Solid State Research Report, Lincoln Laboratory, MIT (1986:3). p. 19.
8. F.R. Nash, J.G. Bergman, G.D. Boyd, and F.H. Turner, *J. Appl. Phys.* **40**, 5201 (1969).



### 3. MATERIALS RESEARCH

#### 3.1 NEW SYSTEM FOR ZONE-MELTING RECRYSTALLIZATION OF SOI FILMS

For the past several years we have prepared silicon-on-insulator (SOI) films in a system<sup>1</sup> that employs the graphite strip-heater technique for zone-melting recrystallization (ZMR).<sup>2</sup> Although this system produces a good yield of device-quality material, it does not yield uniform films routinely, and it cannot be used for processing wafers  $>3$  in in diameter. To overcome these limitations, we have constructed a new strip-heater system that incorporates many improved features and, when suitably fixtured, will have the capability for processing 6-in wafers. This new system has permitted the reproducible preparation of uniformly recrystallized 4-in films and also has led to a significant improvement in the quality of films  $<0.5\text{-}\mu\text{m}$  thick. Figures 3-1 and 3-2 are photographs of the new system's exterior and interior, respectively.

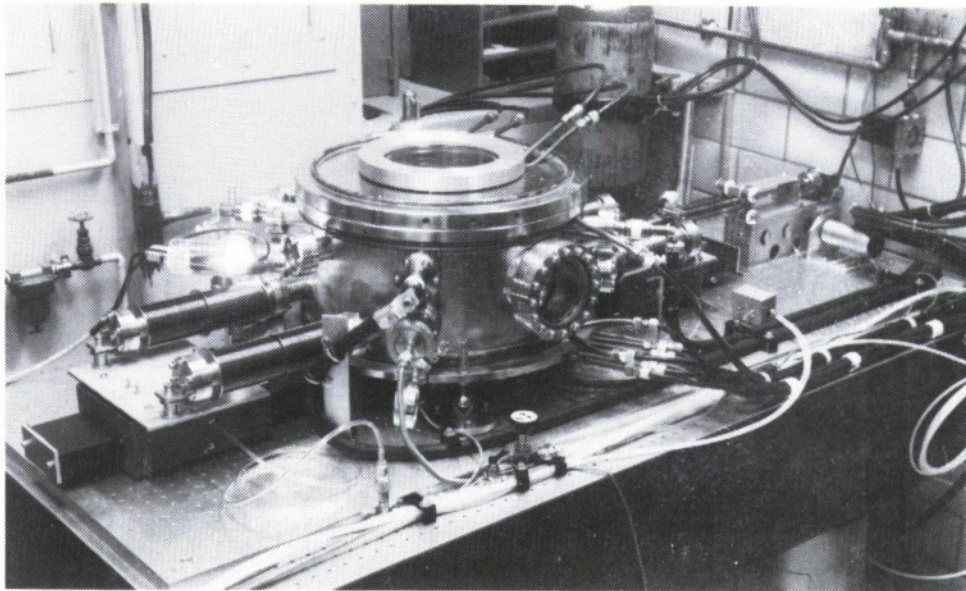
In the ZMR process, a wafer consisting of an encapsulated polycrystalline Si film on a  $\text{SiO}_2$ -coated Si substrate first is heated to a base temperature of  $1100^\circ$  to  $1200^\circ\text{C}$  by radiation from a stationary graphite strip heater located below the wafer. The film then is recrystallized by the passage of a molten Si zone produced by additional radiation from a narrow graphite strip heater that is scanned over the wafer surface. Processing is performed under an Ar atmosphere in a water-cooled, gas-tight chamber. The top cover of the chamber, which is opened for wafer loading, has a large quartz window for observing the recrystallization process.

With the objective of routinely achieving uniform edge-to-edge recrystallization, we adopted the following design goals for the new ZMR system: uniform base temperature over the entire surface of the Si film; constant spacing between the upper strip heater and the wafer surface throughout the heater scan; smooth motion of the liquid-solid interface for scan speeds from  $25\text{ }\mu\text{m/s}$  to  $2.5\text{ mm/s}$ ; and the mechanical, chemical, and thermal stability required for run-to-run reproducibility.

To obtain a uniform base temperature, the wafer is placed on an independently mounted graphite platen rather than directly on the lower heater. The platen, which increases the thermal mass and reduces the effect of radiation from the upper heater on the base temperature, has tantalum heat shields, an auxiliary tungsten-wire ring heater, and a series of nested graphite inserts to minimize radial heat flow. The platen is mounted by means of machined quartz fixtures that provide thermally stable mounting with minimal conductive heat loss. Heat loss from the lower heater to the chamber is reduced by using a series of graphite and tantalum heat shields at the edges and bottom of the heater.

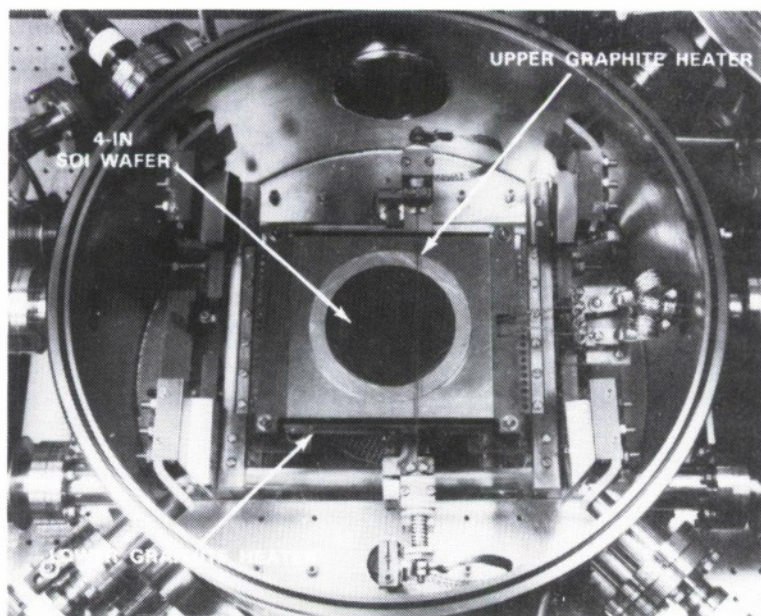
In order to maintain a fixed gap between the upper heater and the wafer surface, the upper and lower heaters are preloaded using tantalum-tungsten alloy springs to accommodate thermal expansion and prevent bowing of the heaters. The platen and upper heater can be positioned independently in order to provide the degrees of freedom necessary to keep the gap constant during scanning.





78872-19

*Figure 3-1. External view of new system for ZMR of SOI films.*



78872-20

*Figure 3-2. Top view of interior of new ZMR system.*

To insure that the solid-liquid interface moves smoothly during ZMR, the new system is designed to minimize jitter in the motion of the upper heater and vibration arising from other sources. The heater strip is clamped at each end to a quartz rod extending in the direction of zone motion. The opposite ends of each quartz rod pass through openings in the chamber wall and into flexible metal bellows that are sealed to the wall by means of flanged metal tubes. Thus, there are two bellows on each side of the chamber. Each bellows is sealed at the far end by a flanged metal plate, and the end of the quartz rod is clamped to this plate. Each pair of flanged plates is mounted on a metal plate attached to a linear air-bearing slide. On one side of the chamber this mounting plate is attached to a high-precision lead screw that is driven by a dc servomotor. By using the air-bearing slides and the bellows, which expand and contract with the motion of the lead screw, this motion is transmitted smoothly to the two quartz rods and thus to the upper heater, while the vacuum integrity of the chamber is maintained without the use of sliding seals or rotary feedthroughs. Several features are incorporated in order to minimize vibration due to sources other than the heater motion: the chamber and drive mechanism are mounted on an isolation table; the turbomolecular pumping system used to evacuate the chamber is mounted directly below the chamber and vibrationally isolated by means of a damped bellows assembly; cooling-water turbulence is reduced by using several parallel water lines with large-bend radii for cooling the chamber and the large O-ring seals between the top cover and chamber body and also between the top cover and quartz viewing window.

The ZMR chamber is basically an ultrahigh-vacuum chamber which provides a clean processing environment and permits the use of commercially available components such as viewports, electrical feedthroughs, and vacuum valves. For long-term stability of the system, all components that are heated to about 500°C or higher during ZMR are fabricated of high-temperature materials, including quartz, boron nitride, alumina, graphite, tantalum, and tungsten. The only other materials used in the chamber are copper and stainless steel, which are thermally shielded, water cooled, or heatsunk to prevent them from being heated to excessive temperatures.

C.K. Chen  
J.W. Caunt

### **3.2 DIFFUSION MODEL FOR ESTIMATING INTERFACE WIDTHS IN HETEROSTRUCTURES GROWN IN A VERTICAL OMVPE REACTOR**

The interface widths in heterostructures grown by organometallic vapor phase epitaxy (OMVPE) are determined by the degree to which abrupt changes in the gas-phase composition introduced at the reactor inlet become broadened by diffusive and convective dispersion. We recently carried out tracer gas experiments to investigate these dispersive effects in a vertical stagnation flow reactor.<sup>3</sup> Step changes in gaseous SF<sub>6</sub> concentration were introduced into a stream of He carrier gas, and the SF<sub>6</sub> concentration just above the susceptor was measured as a function of time for a range of carrier-gas flow rates  $Q$  and inlet-susceptor distances  $L$ . We found that the response time decreases with increasing  $Q$  and decreasing  $L$ . In this report we present a one-dimensional diffusion model, which is consistent with the tracer gas data, for predicting interface widths in heterostructures grown in a vertical reactor.



The physical mechanisms that produce longitudinal dispersion in laminar flows have been studied in detail.<sup>4</sup> When a step change in concentration is introduced at the inlet to a tube, as the gas traverses the tube this step, in general, will be deformed both by molecular diffusion and by convective mixing caused by nonuniformities in the flow. In the ideal case of uniform flow where the velocity  $v$  is constant throughout the tube, there is no convective mixing. The time dependence of the concentration  $C(z,t)$  then is given by

$$\frac{\partial C}{\partial t} + \langle v \rangle \frac{\partial C}{\partial z} = D \frac{\partial^2 C}{\partial z^2} \quad (3-1)$$

where  $z$  is the axial coordinate and  $D$  is the molecular diffusion coefficient. By using the concentration at the inlet as a reference concentration  $C_0$  and the inlet-substrate distance as a length scale  $L$ , Equation (3-1) may be expressed in terms of dimensionless variable as

$$\frac{\partial C^*}{\partial T} + \frac{\partial C^*}{\partial Z} = \text{Pe}^{-1} \frac{\partial^2 C^*}{\partial Z^2} \quad (3-2)$$

where  $C^* \equiv C/C_0$ ,  $T \equiv t\langle v \rangle/L$ ,  $Z \equiv z/L$ , and the molecular Peclet number  $\text{Pe} \equiv \langle v \rangle L/D$ . The Peclet number also can be expressed as  $\text{Pe} = (L^2/D)/(L/\langle v \rangle)$ , the ratio of the diffusion time to the average gas residence time.

The dispersion of a concentration gradient by molecular diffusion has been analyzed by Danckwerts,<sup>4</sup> who solved Equation (3-1) for a step change in concentration propagating in an infinite region of fluid. In this case, the transformation  $z - \langle v \rangle t \rightarrow z$  reduces Equation (3-2) to the one-dimensional diffusion equation, which is solved by a similarity transformation. For a fluid being translated at a velocity  $\langle v \rangle$ , the time dependence of the reduced concentration  $C^*$  at  $L$  is

$$C^*(L,t) = \frac{1}{2} \left( 1 - \text{erf} \frac{1-T}{2 \sqrt{\text{Pe}^{-1} T}} \right) \quad (3-3)$$

The steepness of the concentration change increases with increasing  $\text{Pe}$  because of the associated decrease in the residence time of the gas.

In OMVPE growth, the concentration of a species incorporated in an epilayer generally is proportional to the concentration of the corresponding reactant gas at the growth interface. Therefore, the width of the interface between successive epilayers can be obtained from the time-dependent concentration profile given by Equation (3-3), which can be written as

$$1 - 2C^*(L,t^*) = \text{erf } \zeta^* \quad (3-4)$$

where  $t^*$  is the time at which  $C^*$  at  $L$  equals a specified fraction  $x$ , and  $\zeta^*$  is given by

$$\zeta^* = \frac{L - t^* \langle v \rangle}{2 \sqrt{Dt^*}} \quad (3-5)$$

Solving for  $t^*$  gives

$$t^* = \frac{L}{\langle v \rangle Pe} \left( Pe + 2\zeta^{*2} - 2\zeta^* \sqrt{Pe + \zeta^{*2}} \right) \quad (3-6)$$

Since the error function is symmetric, the time interval over which  $C^*$  varies from  $x$  to  $(1 - x)$  is

$$\Delta t^* = \frac{4L\zeta^*}{\langle v \rangle Pe} \sqrt{Pe + \zeta^{*2}} \quad (3-7)$$

We define a transition width  $w$  as the distance over which  $C^*$  exhibits this variation. For a constant growth rate  $V_g$ ,  $w = V_g \Delta t^*$ . From Equation (3-7)

$$\frac{w}{L} = \frac{4\zeta^*}{RPe} \sqrt{Pe + \zeta^{*2}} \quad (3-8)$$

where  $R \equiv \langle v \rangle / V_g$ . For a fixed gas flow rate and constant  $Pe$ , Equation (3-8) implies that arbitrarily small values of  $w/L$  are obtained only by decreasing the growth rate, i.e.,

$$(w/L) \rightarrow 0 \text{ as } R \rightarrow \infty$$

For comparing theory with experiment, we take the interface width  $W$  to be the value of  $w$  for  $x = 0.1$ , i.e., the distance over which the reduced composition  $C^*$  varies from 0.1 to 0.9 ( $\zeta^* \approx 0.9$ ). Equation (3-8) has been used to calculate  $W$  as a function of carrier-gas flow rate  $Q$  for  $L = 4$  and  $16$  cm,  $V_g = 1$  cm/s, and  $D = 0.4$  cm<sup>2</sup>/s, the diffusivity of  $SF_6$  in He at atmospheric pressure. The calculated curves are plotted in Figure 3-3, which also shows the “measured” interface widths that were determined from the time intervals required for the  $SF_6$  concentration measured at the susceptor to increase from 10 to 90 percent of the inlet concentration. As expected,  $W$  decreases with increasing  $Q$  and decreasing  $L$ . The dependence of “measured”  $W$  on  $Q$  and  $L$  is consistent with the model even though the convective contribution to the dispersion was neglected.

Equation (3-8) has been used to calculate the dependence of  $W$  on  $Q$  for GaAs/AlGaAs heterostructures grown in a vertical stagnation flow reactor 10 cm in diameter operating at a reduced pressure of 0.1 atm. For  $L = 16$  cm,  $V_g = 10$  Å/s, and values of  $D$  between 0.2 and 4 cm<sup>2</sup>/s (a range that includes the diffusivities of trimethylgallium and trimethylaluminum in hydrogen), interface widths on the order of a few monolayers are predicted for values of  $Q >$  about 6 slpm, as shown in Figure 3-4.

C.A. Wang

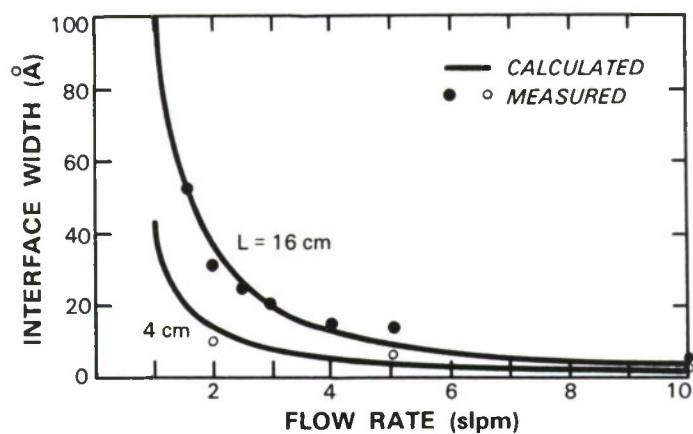


Figure 3-3. Calculated and "measured" interface widths in  $\text{SF}_6$  tracer gas studies, plotted as a function of flow rate for inlet-susceptor distances of 4 and 16 cm.

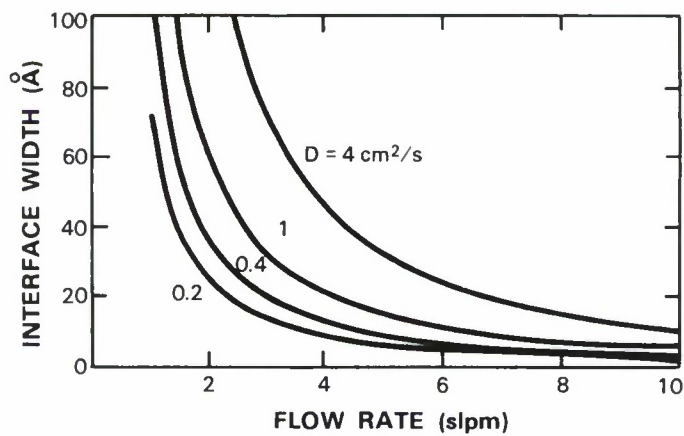


Figure 3-4. Interface width in GaAs/AlGaAs heterostructures calculated as a function of hydrogen flow rate for inlet-susceptor distance of 16 cm, growth rate of  $10 \text{ Å/s}$ , and diffusivity range for trimethylgallium and trimethylaluminum in hydrogen.



## REFERENCES

1. J.C.C. Fan, B-Y. Tsaur, R.L. Chapman, and M.W. Geis, Appl. Phys. Lett. **41**, 186 (1982), DTIC AD-A153719.
2. J.C.C. Fan, B-Y. Tsaur, and M.W. Geis, J. Cryst. Growth **63**, 453 (1983), DTIC AD-A147189.
3. Solid State Research Report, Lincoln Laboratory, MIT (1986:3), p. 23.
4. See, for example, P.V. Danckwerts, Chem. Eng. Sci. **2**, 1 (1953).

## 4. MICROELECTRONICS

### 4.1 LASER-DIRECT-WRITTEN TUNGSTEN MICROSTRIP LINES FOR GaAs MONOLITHIC MICROWAVE INTEGRATED CIRCUIT TRIMMING

Inadequate processing control can cause variations in device and circuit parameters which degrade performance of a GaAs monolithic microwave integrated circuit (MMIC). In most instances the performance of an MMIC can be improved by circuit trimming after fabrication. In this report we demonstrate a new tuning technique using laser-direct-written W lines which provides fast, versatile, and damage-free tuning of GaAs MMICs without the incorporation of any prefabricated special tuning structures.

Laser-direct-written Si and W lines already have been used in Si integrated circuits to customize commercial CMOS gate arrays.<sup>1</sup> The specific reaction chosen for the present application is based on pyrolytic tungsten deposition from tungsten hexafluoride, initiated with 488-nm-wave-length light from an argon-ion laser.<sup>2</sup> Thermal-bias experiments indicate that the initiation temperature is approximately 200°C, suggesting that the trimming process will not disturb active circuit components.

The Ti-Au (2  $\mu\text{m}$  Au on 70 nm Ti) microstrip lines were defined on a 125- $\mu\text{m}$ -thick semi-insulating GaAs substrate by photoresist lift-off, and a layer of  $\sim 1\text{-}\mu\text{m}$ -thick polyimide was patterned so that only the Ti-Au metallization was uncovered. The polyimide was cured at 300°C after patterning. The W lines then were written on the polyimide and connected to the Ti-Au. In Figure 4-1(a), a scanning electron micrograph (SEM) shows the connection of a laser-written W microstrip line to the Ti-Au metallization. Figure 4-1(b) shows that the W film conforms to an etched step in a GaAs substrate. Therefore, this direct-writing technique can be applied to a GaAs chip having nonplanar features, such as mesas and capacitors with thick dielectric layers. The minimum linewidth achievable by this laser-writing process is 2  $\mu\text{m}$ , and the sample stage can be controlled to a position accuracy of 0.1  $\mu\text{m}$ . The scanning speed of laser writing is 100  $\mu\text{m/s}$ .

Figure 4-2 is an SEM of a W matching stub connected to a Ti-Au microstrip line. The W metallization is 1.8- $\mu\text{m}$  thick, 50- $\mu\text{m}$  wide, and 1.65-mm long, which is equal to one-quarter wavelength at 16 GHz.

Scattering parameters were measured using a network analyzer and  $|S_{21}|$  is plotted vs frequency in Figure 4-3. The resonant frequency of 15.9 GHz is very close to the design frequency of 16 GHz and the measured quality factor is 11. Super-compact was used to extract the parameters of the W lines from the measurement. The calculation indicates that at 16 GHz the loss for the 50- $\Omega$  microstrip line is 2.6 dB/cm, approximately three times higher than for the 50- $\Omega$ , Ti-Au microstrip line. The higher loss can be attributed to the higher resistivity ( $\approx 30\text{ }\mu\Omega\text{-cm}$ ) of the W. For most trimming applications this additional loss is insignificant because of the short lengths required. A thicker W microstrip line would reduce the resistance, thus further lowering the loss. For a microstrip line consisting of many overlapped W lines, the effective thickness can be

increased easily by increasing the overlap between adjacent lines or by using multiple passes to stack layers of laser-written W.

Our current experiments show that an open stub can be introduced with a wide range of impedance values at any location in an existing microstrip circuit without prior provision, such as prefabricated trimming tabs. In addition, the impedance of a selected portion of an existing microstrip line can be changed by widening the linewidth using the W film. If metal pads for trimming are already on the substrate, the W lines can easily be used to connect them. The trimming procedures can be accomplished on either a single die or a whole wafer, and are reversible because the W line can be disconnected using laser-cutting techniques.

C.L. Chen	W.E. Courtney
J.G. Black	D.J. Ehrlich
L.J. Mahoney	R.A. Murphy
S.P. Doran	

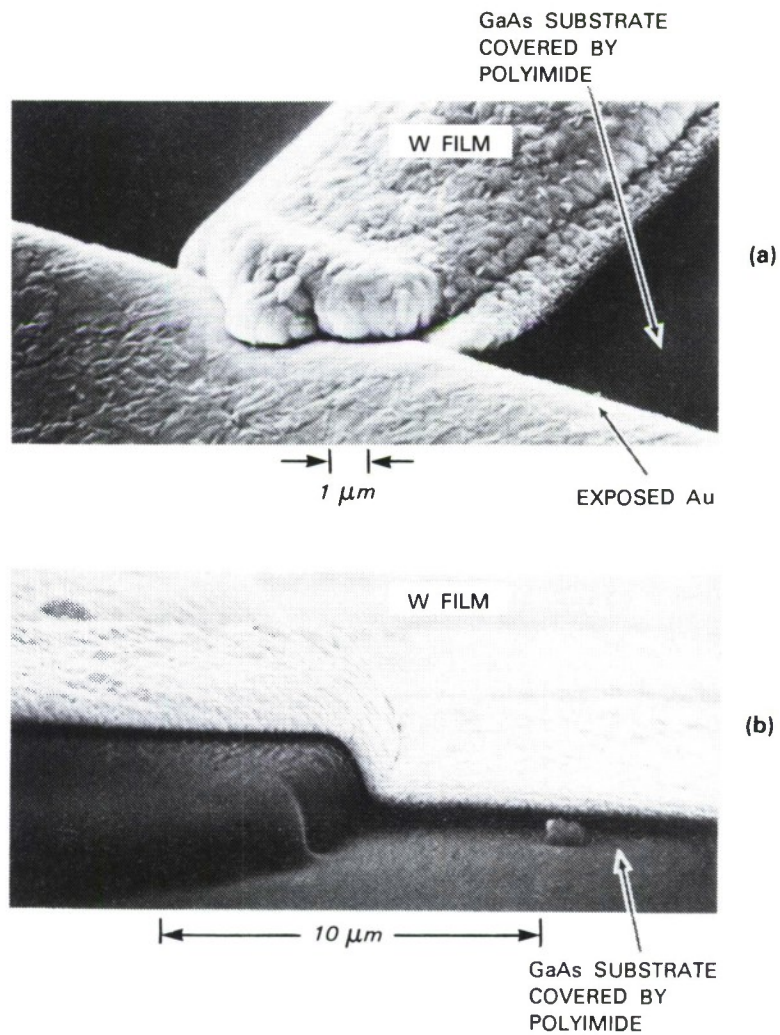


Figure 4-1. SEM of laser-direct-written W lines. (a) Connection of a W line to Ti-Au metallization. (b) W film conforming to an etched step on GaAs substrate.

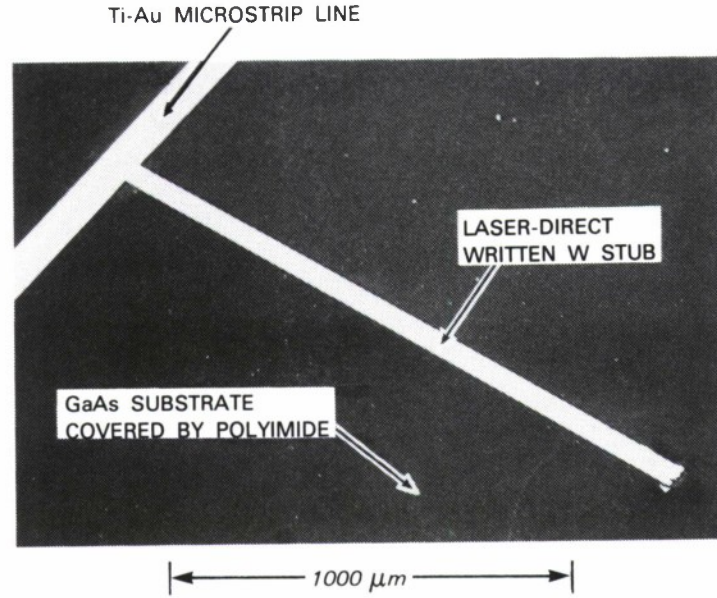


Figure 4-2. SEM of a W open-circuit stub connected to a Ti-Au microstrip line. Entire GaAs substrate except area of Ti-Au metallization is covered by a polyimide layer.

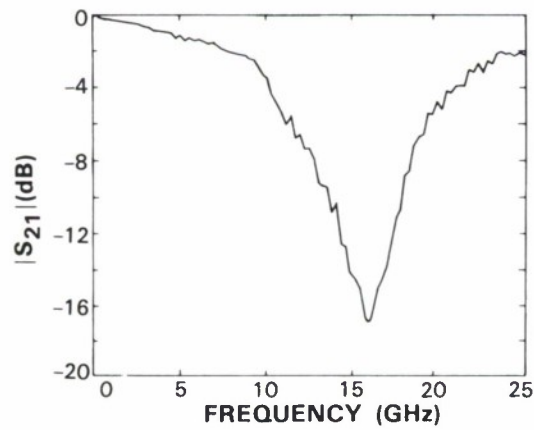


Figure 4-3. Measured  $|S_{21}|$  of circuit shown in Figure 4-2.



## 4.2 SMALL-SIGNAL GAIN PERFORMANCE OF THE PERMEABLE-BASE TRANSISTOR AT EHF

We present here the first-reported results for a permeable-base transistor (PBT) amplifier operating in the EHF region of the frequency spectrum. PBTs having a base grating of 3200-Å periodicity and 1-mm periphery were mounted into specially developed EHF circuit fixtures and characterized over the 33- to 50-GHz frequency band using an EHF vector network analyzer. From the de-embedded device scattering parameters, a narrowband small-signal amplifier design was calculated and realized.

Figure 4-4 shows scattering-parameter data typical of these devices over the 39- to 47-GHz frequency range. The nonmonotonic phase variation apparent in the measured  $S_{11}$  parameter in Figure 4-4(a) can be attributed to the effects of bond-wire reactances and variations in calibration standards. The devices generally exhibited favorable characteristics for an EHF amplifier design. The input and output impedance levels were moderate, facilitating the design of matching networks. The devices demonstrated excellent unilateral properties ( $|S_{12}| < -25$  dB) which reduce interaction between the load and input circuits and permit greater circuit design flexibility.

A simple narrowband amplifier, using only shunt open stubs, was designed using the measured scattering parameters for a selected device. The resulting amplifier/circuit mount is shown in Figure 4-5. The circuit consists of input and output microstrip matching networks fabricated on 250- $\mu$ m-thick alumina substrates.

The small-signal gain performance of the amplifier, corrected for substrate and mount losses, is shown in Figure 4-6. These circuit losses degrade amplifier gain by  $\sim 1$  dB. Maximum gain for the amplifier was 11 dB measured at 40.5 GHz for a small-signal drive input. This result represents the first-reported amplifier demonstration for the GaAs PBT in an EHF circuit. The amplifier matching networks were designed from the measured scattering-parameter data at 40.5 GHz and did not require extensive empirical tuning to achieve the described performance.

The PBT offers a number of advantages for EHF circuit design, including state-of-the-art gain, moderate impedance levels per unit grating periphery, and a highly unilateral characteristic. A design effort is underway currently to incorporate these devices into a multistage broadband amplifier in the 40-GHz frequency band.

R. Actis	B.J. Clifton
R.W. Chick	K.B. Nichols
M.A. Hollis	C.O. Bozler

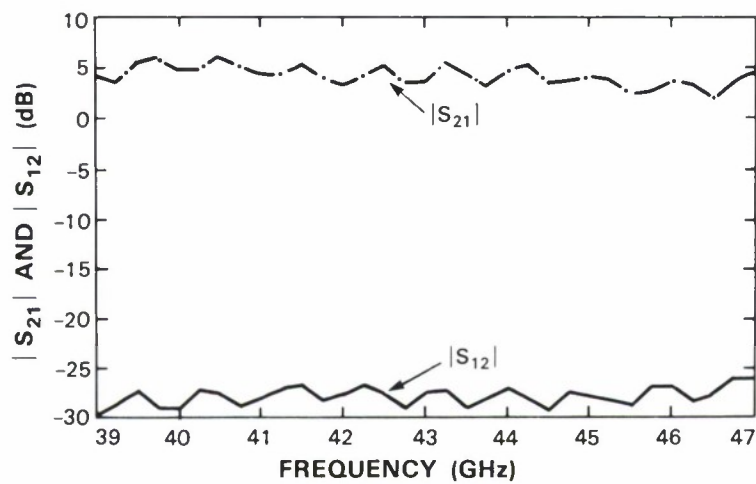
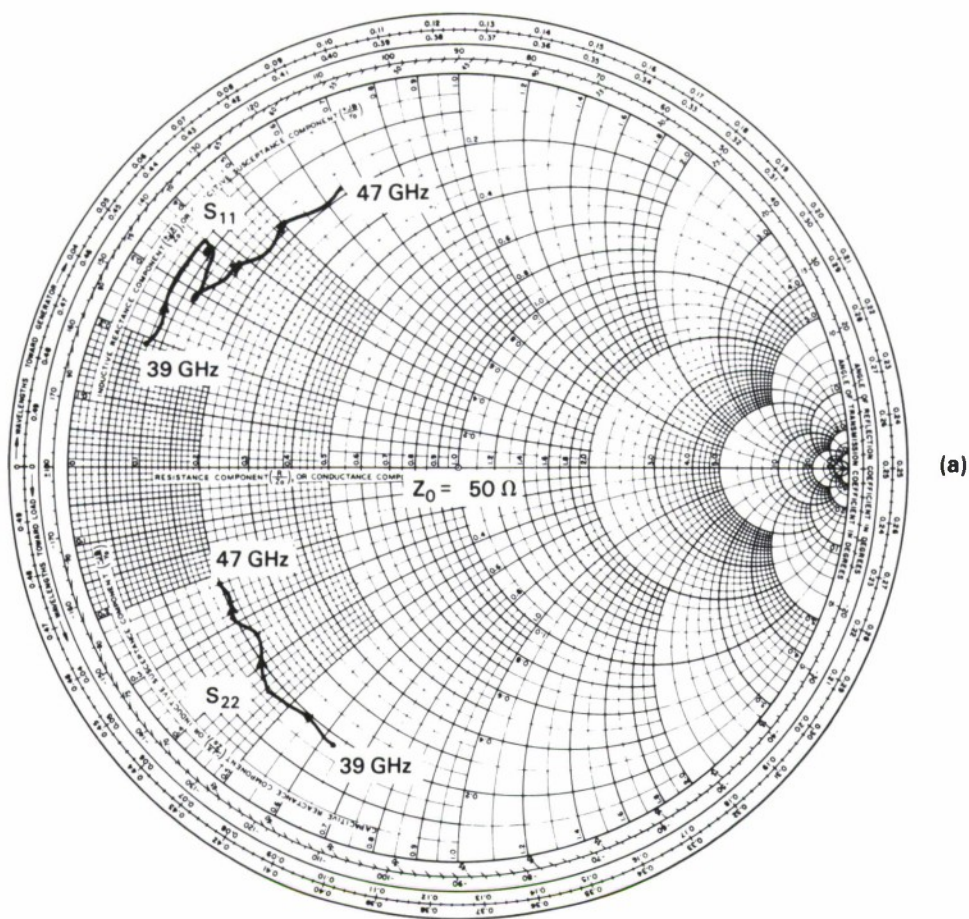


Figure 4-4. Measured small-signal scattering parameters of PBT embedded in a 50- $\Omega$  system. (a)  $S_{11}$  and  $S_{22}$  with 50- $\Omega$  normalization impedance. (b)  $|S_{12}|$  and  $|S_{21}|$  in decibels.

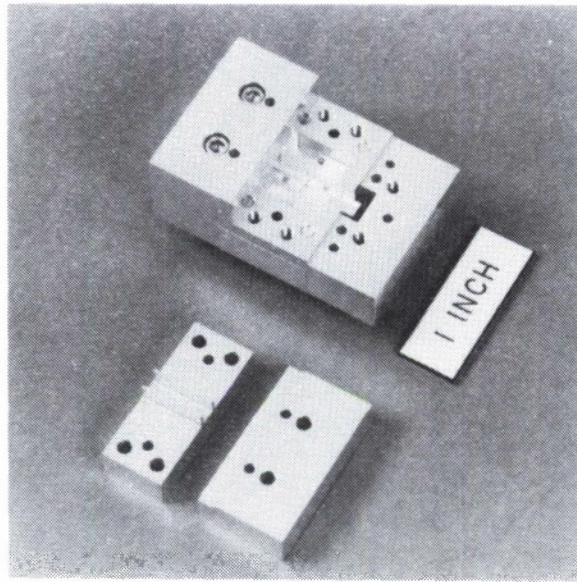


Figure 4-5. PBT amplifier circuit embedded in EHF mount.

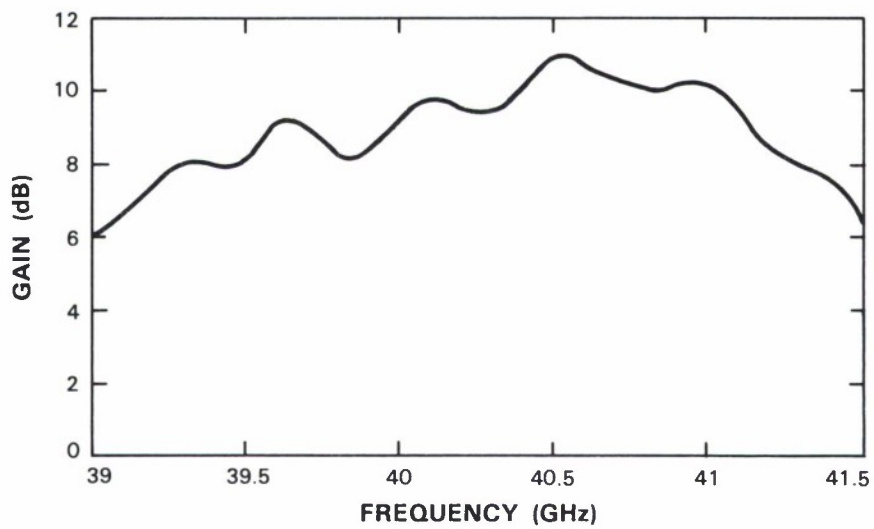


Figure 4-6. Small-signal gain performance of a single-stage PBT amplifier. Substrate and mount losses have been removed from data.



### 4.3 PBT SAMPLE-AND-HOLD CIRCUITS

Many applications exist for ultrahigh-speed sample-and-hold circuits in analog-to-digital (A/D) conversion of signals having bandwidths of 5 GHz and higher. Current commercially available A/D converters operate only up to about 200 MHz. The PBT is an ideal candidate for the switching transistor in a high-speed sample-and-hold circuit because of its very fast transistor switching speed, low on-state resistance, and minimal feedthrough in the off state.<sup>3-5</sup> These properties result from the unique structure of the PBT.

A first attempt at making a sample-and-hold circuit using the PBT is shown in Figure 4-7. It consists of a 50- $\Omega$  coplanar-waveguide circuit and uses coaxial launchers on the input, output, and signal terminals. Figure 4-8 shows the arrangement of the peripheral electronics, including the pulser, signal to be sampled, and oscilloscope. The sampling rate provided by this instrumentation is 10 MHz, and the signal to be sampled can range from 100 MHz to 5 GHz in frequency. Figure 4-9 is a schematic showing how the input signal is sampled by the lower-frequency sampling pulse giving an output signal which steps through the sine wave at the beat frequency. Figure 4-10 shows the output waveform for an input of 2, 4, and 5 GHz. In these initial measurements no effort was made to provide an impedance match at the input. This causes the output signal to have lower amplitude and to be out of phase with the input. We are beginning experiments on a new circuit that has better impedance match and lower feedthrough, the latter as a result of reducing the resistance in the ground path.

These sample-and-hold circuits must be treated as microwave circuits because of the very large operational bandwidths. Since the current devices are on chips with the emitter contact on the back, they can be mounted easily in a coplanar-waveguide circuit. The coplanar-waveguide configuration is convenient because it provides easy access to the circuit ground for the hold capacitor, while also providing a 50- $\Omega$  waveguide to match the sampling pulse generator and the output measuring equipment. A high-speed multiplexer could be built by placing a number of the coplanar circuits just described, side-by-side on a ceramic, or eventually on a GaAs semi-insulating substrate. The inputs of the coplanar circuits are common and the outputs feed separately into slower silicon-based A/D circuits. By providing the switching signal from a single source with an appropriate delay to each coplanar circuit, each sample-and-hold circuit sequentially would sample the input signal.

C.O. Bozler	W.H. McGonagle
R.H. Mathews	K.B. Nichols
M.S. DiIorio	M.A. Hollis

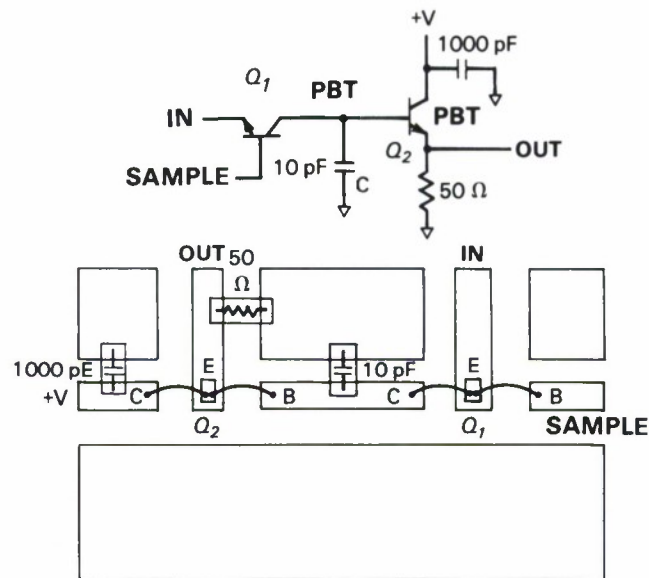


Figure 4-7. Circuit schematic and coplanar-waveguide layout for PBT sample-and-hold circuit.

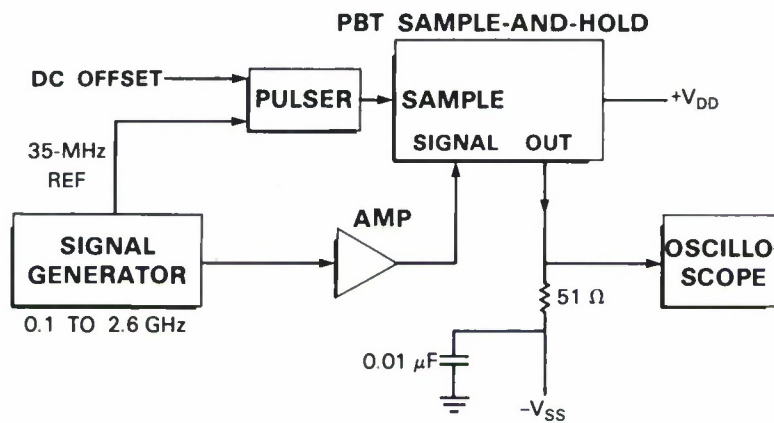


Figure 4-8. Sample-and-hold measurement system.



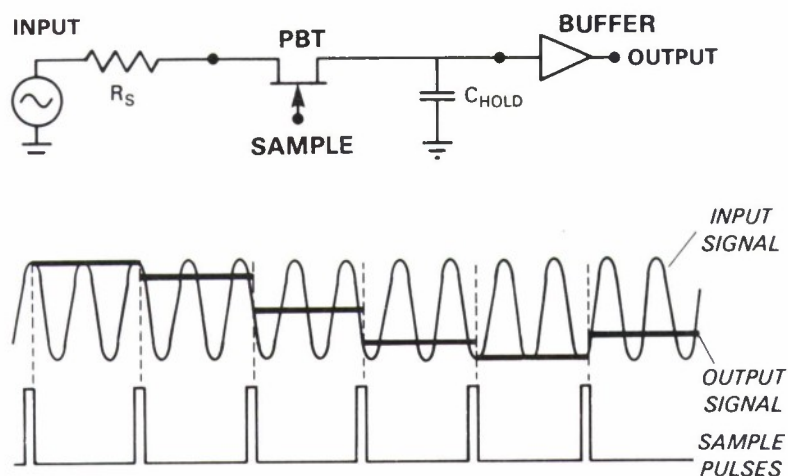


Figure 4-9. PBT sample-and-hold circuit schematic with input signal, output signal, and sample pulses.

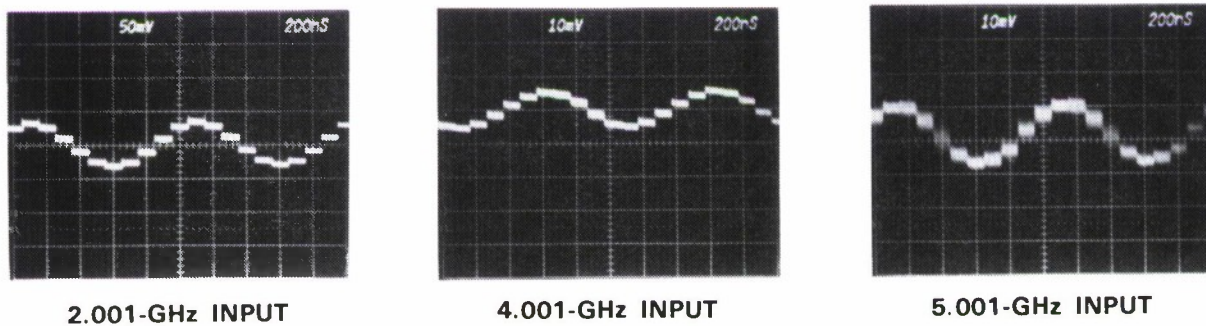


Figure 4-10. Measured output signal for PBT sample-and-hold for 2-, 4-, and 5-GHz input signal.

#### 4.4 FABRICATION OF SUBMICROMETER-SIZE STRUCTURES IN Si USING SF<sub>6</sub>/O<sub>2</sub> REACTIVE ION ETCHING

Submicrometer structures having high aspect ratios have been etched with high rates in Si using reactive-ion etching (RIE) in a SF<sub>6</sub>/O<sub>2</sub> mixture. We have etched 320-nm-periodicity straight-walled grooves in Si at etch rates exceeding 60 nm/min with selectivity >10:1 with respect to SiO<sub>2</sub>. The anisotropic RIE process for etching Si described here differs from that previously reported in that we have added O<sub>2</sub> to SF<sub>6</sub> to control the anisotropy. Although others have found that the high degree of anisotropy needed to etch fine structures in Si with SF<sub>6</sub> can be achieved by adding C- or Cl-containing gases to SF<sub>6</sub>, undesirable polymers were formed on the etched sidewalls and only relatively low etch rates were achieved.<sup>6,7</sup> In this report, we demonstrate that a combination of O<sub>2</sub> partial pressure, system pressure, and target bias voltage exists which achieves a high degree of anisotropy and a high etch rate without sidewall polymerization.

The etching system has been described previously.<sup>8</sup> All samples were placed on the powered electrode with a quartz plate on the electrode. Submicrometer patterns were fabricated using X-ray lithography and lift-off of Cr; larger patterns were fabricated using conventional photolithography and lift-off of Ni.

Figure 4-11 shows the Si and SiO<sub>2</sub> etch rates as a function of O<sub>2</sub> concentration in the etching system. The bias voltage, system pressure (30 mTorr), and SF<sub>6</sub> flow rate (5 sccm) were held constant. The Si etch rate decreases from 500 nm/min for pure SF<sub>6</sub> to 60 nm/min for a 33-percent SF<sub>6</sub>/O<sub>2</sub> mixture. The SiO<sub>2</sub> etch rate is more than an order of magnitude lower than the Si etch rate for all mixtures tested. We did not observe the increase in etch rate for small additions of O<sub>2</sub> which has been reported by others.<sup>9,10</sup> We believe that the relatively low system pressure and the O<sub>2</sub> liberated by the etching of the quartz plate cause O<sub>2</sub> to compete with F for Si sites, which results in a decrease of the Si etch rate.

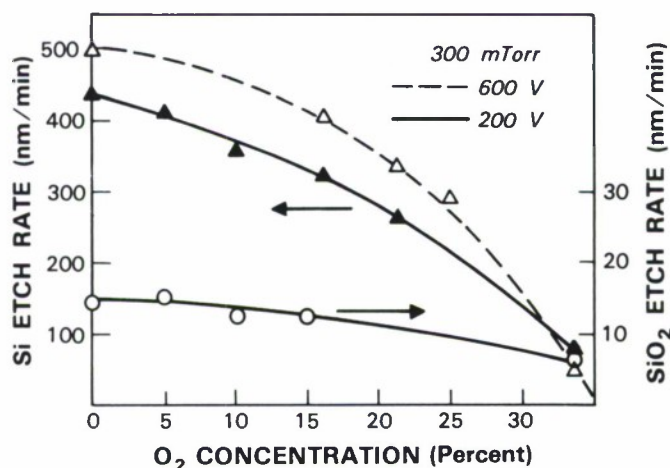


Figure 4-11. Etch rates of Si and SiO<sub>2</sub> as a function of O<sub>2</sub> concentration in etching system. System pressure and dc bias voltages are indicated.

The effect of  $O_2$  concentration on the etching profile is demonstrated by Figure 4-12. For concentrations of  $O_2$  ranging from 0 to 15 percent, nearly isotropic profiles are observed. For higher concentrations, the profiles become more anisotropic. Figure 4-13 shows the anisotropic etching of 100-nm-wide lines (320-nm periodicity) which have been etched to a depth of 500 nm in Si with little or no undercutting. In this experiment, an  $O_2$  concentration of 33 percent was used with a bias voltage of 300 V. We believe that this relatively high  $O_2$  concentration, at this system pressure and bias voltage, results in reduced Si etch rates of the sidewall because of surface oxidation, and provides a high degree of anisotropy.

We have succeeded in etching submicrometer-size features in Si by adding  $O_2$  to  $SF_6$  in an RIE mode. High etch rates of 60 nm/min, aspect ratios  $>6:1$ , and high selectivity to  $SiO_2$  have been achieved without detrimental sidewall polymerization. This represents a useful process for etching VLSI patterns in Si on  $SiO_2$ .

A.R. Forte  
D.D. Rathman

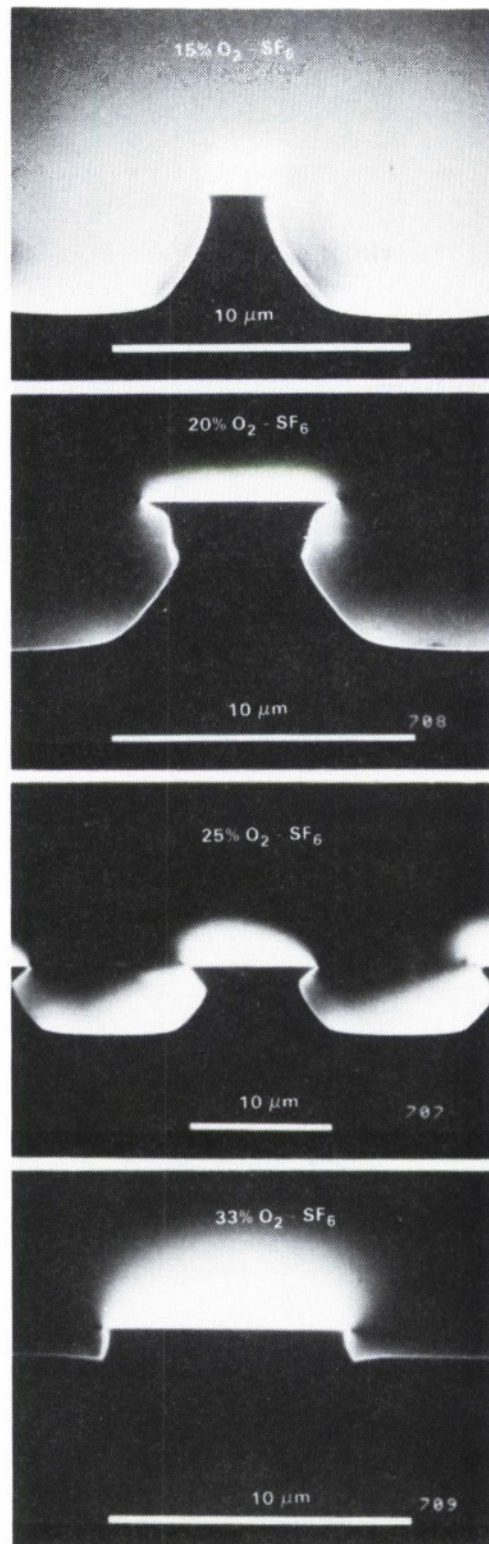
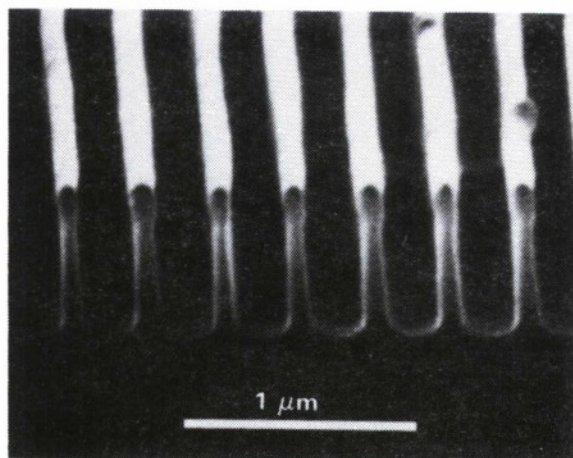


Figure 4-12. Si etch profiles for several  $\text{SF}_6/\text{O}_2$  mixtures.



*Figure 4-13. SEM of a grating with 100-nm lines and 220-nm spaces etched in Si.*



## REFERENCES

1. D.J. Ehrlich, J.Y. Tsao, D.J. Silversmith, J.H.C. Sedlacek, R.W. Mountain, and W.S. Graber, IEEE Electron Device Lett. **EDL-5**, 32 (1984), DTIC AD-A153146.
2. J.G. Black, D.J. Ehrlich, M. Rothschild, S.P. Doran, and J.H.C. Sedlacek, to be published in J. Vac. Sci. Technol. B **5** (1987).
3. C.O. Bozler, M.A. Hollis, K.B. Nichols, S. Rabe, A. Vera, and C.L. Chen, IEEE Electron Device Lett. **EDL-6**, 456 (1985).
4. M.A. Hollis, K.B. Nichols, R.A. Murphy, R.P. Gale, S. Rabe, W.J. Piacentini, C.O. Bozler, and P.M. Smith, IEDM Tech Dig., 102 (1985).
5. C.O. Bozler and G.D. Alley, IEEE Trans. Electron Devices **27**, 1128 (1980), DDC AD-A096619.
6. M. Mieth and A. Barker, Semiconductor International **7**, No. 5, p. 222 (1984).
7. K.S. Uhm, M.R. Kump, J.P. McVittie, and R.W. Dutton, in *Process Simulators for Si VLSI and High Speed GaAs Devices* (Stanford University Press, Stanford, 1986), p. 253.
8. S. Cabral, M. Elta, and A. Chu, Elec. Chem. Soc. Proceed. **82-1**, 348 (1982).
9. R. d'Agostino and D. Flamm, J. Appl. Phys. **52**, 162 (1981).
10. R. Kawabata, D. Kimura, H. Komiya, and H. Shimizu, Sharp Technical J. (Japan) **33**, 47 (1985).

## 5. ANALOG DEVICE TECHNOLOGY

### 5.1 INCREMENTAL WRITING IN MNOS CAPACITORS

The associative memory proposed by Sage *et al.*<sup>1</sup> relies on the storage of analog information in reprogrammable nonvolatile memory elements, in particular metal-nitride-oxide-silicon (MNOS) devices. We now have demonstrated a technique for incremental writing which would allow the analog data in each memory site to be updated without executing a complete erase-write cycle.

Our test structures are the simple dual-dielectric (600 Å  $\text{Si}_3\text{N}_4$ /25 Å  $\text{SiO}_2$ ) capacitors described by Withers *et al.*<sup>2</sup> and fabricated in p-type Si. Under normal operation the device is first erased to a known state (flatband voltage  $V_{\text{FB}} \approx -5.5$  V) by the application of a large negative pulse (–35 V) to the gate. For writing, a large ( $\approx 40$  V) positive bias is applied which depletes the Si under the gate. In the absence of signal input, represented by electrons in an inversion layer, almost all the gate bias is dropped across this depletion region and the electric field in the oxide is low. When a known signal-charge packet is injected (in our case, photogenerated electrons), the depletion region collapses somewhat and the field across the oxide increases in near proportion to the number of charges injected. Tunneling of the signal charge to traps in the nitride occurs when the oxide field is greater than a threshold value. Correspondingly, nearly independently of gate bias, a minimum number of electrons (the “fat zero”) must be present for tunneling to take place. Thus, there will be charge storage in the nitride and the accompanying shift in the flatband voltage only when the injected charge packet is greater than this fat zero. Furthermore, the tunneling process stops when all but the fat-zero charge has tunneled. Over a wide range, the flatband-voltage shift essentially is proportional to the input charge packet, as demonstrated by Withers *et al.*<sup>2</sup> For most analog applications one can operate in the linear range and compensate for the fat zero by providing bias charge.

For associative-memory applications it is desirable to be able to accumulate successive independent analog data samples. This incremental writing requires that an input charge packet be added to the previously stored packets within the silicon nitride. Under these conditions, the effect of the fat zero is important and has to be taken into account.

Our experiments were designed to help us gain a better understanding of the incremental writing process. Figure 5-1 shows the results of our experiments. The leftmost curve is obtained by operating a test capacitor as described in Reference 2. In order to reach a known erased state, we cycle the device by erasing (with a –35-V, 600-ms pulse), then writing to saturation (with a +35-V, 600-ms pulse and a large injected charge packet), and again erasing. The result of this erase sequence is a state in which the minority carriers (electrons) have backtunneled from the nitride to the silicon while some majority carriers (holes) have tunneled and are trapped in the nitride, producing a distribution of the two carriers in the nitride which is independent of previously stored information. Once the device is thus erased, we write the signal-charge packet. The resulting flatband-voltage shift is plotted as a function of the signal-packet size in Figure 5-1

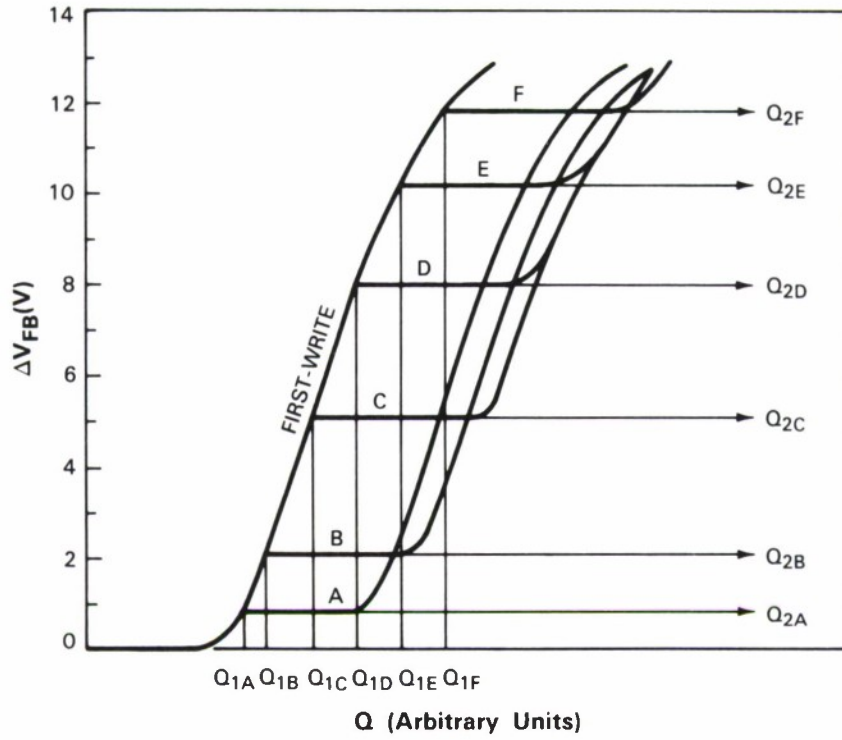


Figure 5-1. Flatband-voltage shift  $\Delta V_{FB}$  plotted as a function of signal-charge packet. Leftmost curve is obtained when device is erased to a known state and written with a signal-charge packet  $Q_{1A}$ ,  $Q_{1B}$ ,  $Q_{1C}$ ,  $Q_{1D}$ ,  $Q_{1E}$ , and  $Q_{1F}$ . Remaining curves result from incremental writing and show flatband-voltage shift plotted as a function of second charge packet,  $Q_{2A}$ ,  $Q_{2B}$ ,  $Q_{2C}$ ,  $Q_{2D}$ ,  $Q_{2E}$ , and  $Q_{2F}$ , plotted on displaced abscissas with origins at corresponding first-packet size.

(leftmost curve). From the plot we see that there is a minimum charge packet required before any shift is produced (fat zero), followed by a linear region, and eventually a saturation region.

The remaining curves in Figure 5-1 are the result of incremental writing. The incremental-writing sequence consists of the erase cycle just described, followed by the two write operations during which two independent charge packets are injected. Between the write operations, the gate is pulsed sufficiently negative to accumulate the Si surface and remove any inversion-layer electrons (e.g., the fat-zero charge), but not strongly enough to cause any tunneling. The curves show the flatband-voltage shift plotted as a function of the second charge packet when the first one is kept at the constant values  $Q_{1A}$ ,  $Q_{1B}$ ,  $Q_{1C}$ ,  $Q_{1D}$ ,  $Q_{1E}$ , or  $Q_{1F}$ . For example, curve C is obtained by erasing the device and writing with a first packet of size  $Q_{1C}$ . A second write then is performed with a charge packet of variable size  $Q_{2C}$  indicated on the displaced axis  $Q_{2C}$ . The measurement is repeated with a range of  $Q_{2C}$  values to map out the curve C. The curves A, B, C, D, E, and F (corresponding to different first-packet sizes) are parallel to each other and get closer together until eventually they overlap (for initial charge  $>Q_{1C}$ ). The horizontal displacement of these curves from the first-write (leftmost) curve is the fat zero associated with the second write. Corresponding to the converging displacement, the fat zero  $\Delta Q$  of the second writing operation increases with the first-packet size  $Q_1$  until it reaches a constant value as shown in Figure 5-2.

This result is also valid for subsequent multiple-writing operations. In general, we see that incremental writing is possible and can be controlled; by adding the fat zero corresponding to the initial state, the result of successive writing operations follows closely the original  $V_{FB}$  vs  $Q$  curve.

A.L. Lattes

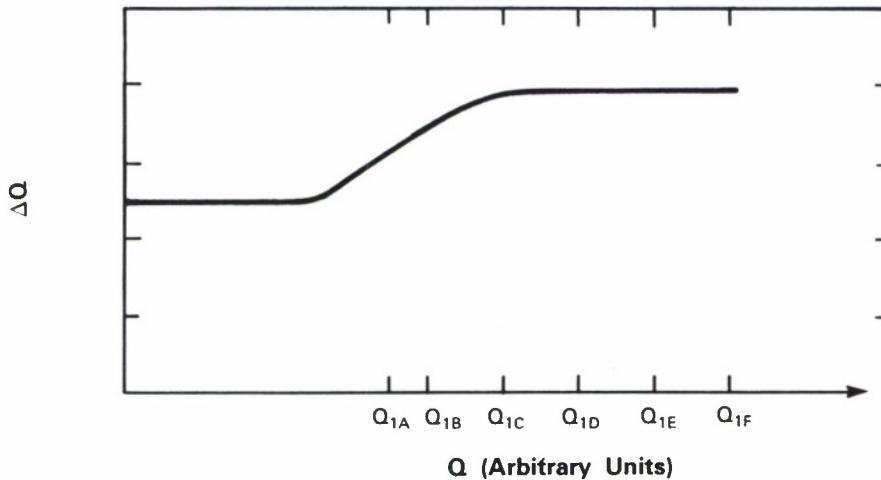


Figure 5-2. Fat zero  $\Delta Q$  of second writing operation as a function of first signal-charge packet. Fat zeros represent displacement of second-write curves in Figure 5-1 from first-write curves.



## 5.2 LASER PHOTOCHEMICAL PROCESSING OF Cr-Cr<sub>2</sub>O<sub>3</sub> FILMS FOR AMPLITUDE COMPENSATION OF SURFACE-ACOUSTIC-WAVE DEVICES

A previous attempt<sup>3</sup> to use laser-direct-write techniques to modify the surface-acoustic-wave (SAW) attenuation of films dc-sputtered from Cr-Cr<sub>2</sub>O<sub>3</sub> (cermet) targets failed to produce observable effects. However, an improved reaction cell and vacuum system, as well as the ability to more precisely meter gas flow, have provided for a system whereby cermet properties can be predictably and favorably altered.

Laser-direct-write processing of SAW-attenuating films is evaluated using delay lines fabricated on YZ-LiNbO<sub>3</sub>. A strip  $\sim 50 \lambda_c$  wide, where  $\lambda_c$  is the midband acoustic wavelength, is deposited between transducer pairs. Cermet resistivity, hence attenuation, is successfully modified by raster scanning the focused argon-laser beam across the surface in the presence of selected gases at total pressures ranging from below 1 to over 600 Torr.

A typical "as-deposited" film is characterized by a dc sheet resistance of  $2 \text{ M}\Omega/\square$ , producing an attenuation of  $0.36 \text{ dB}/\lambda$  and a phase change of  $0.8^\circ/\lambda$ . When exposed to focused 488-nm laser radiation in a low-pressure ambient of O<sub>2</sub>, the film is rendered highly resistive, with the measured dc resistivity increasing by several orders of magnitude. As is characteristic of insulating films, the modified cermet provides essentially no attenuation or phase change to SAWs.

The measured dc sheet resistance for a film processed at several O<sub>2</sub> pressure levels is plotted in Figure 5-3. This measurement was obtained, at each selected pressure level, by laser processing a  $50\text{-}\mu\text{m}$  strip outside the acoustic-beam path, as diagrammed in the insert.

Scanning electron micrographs of the laser-modified cermet show no morphological change to the surface. Auger analysis revealed no measurable compositional differences throughout the thickness of the film. Cermet films processed in Cl<sub>2</sub> ambient, which exhibited the same decreases in attenuation, showed residual Cl only at the very surface.

Additionally, cermet films similarly processed in a vacuum ( $<6 \times 10^{-2}$  Torr) or an Ar environment became more electrically conductive. The modified film provided a phase change of approximately  $9^\circ/\lambda$ , accompanied by a small decrease in acoustic attenuation. A more thorough characterization of this process is scheduled. If the correct cermet thickness and processing techniques are developed, they would provide complete phase and amplitude compensation by a single cermet film processed alternately in Ar or O<sub>2</sub>.

Figure 5-4 shows calculated<sup>4</sup> acoustic attenuation and phase change expected from a resistive film on YZ-LiNbO<sub>3</sub> as a function of the ac sheet resistivity. Indicated are the "as-deposited" cermet dc resistance value of  $2 \text{ M}\Omega/\square$  and the post-processing value of  $400 \text{ M}\Omega/\square$ . Favorable comparison between measured and calculated acoustic response characteristics indicate that the effective sheet resistance of the film at 150 MHz is similar to the measured dc sheet resistance. The resistivity value shown for the film processed in a vacuum was not measured but instead was estimated from the measured acoustic characteristics of the film.

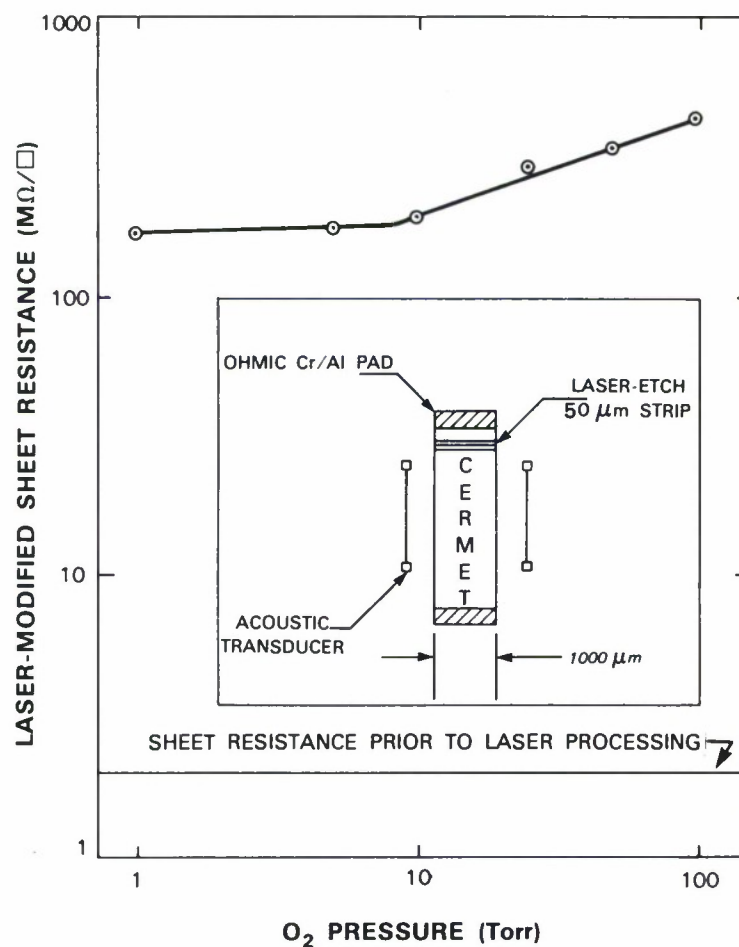


Figure 5-3. Dc sheet resistance of cermet (Film 1) laser-modified in O<sub>2</sub> ambient for selected range of total gas pressure within reaction cell. Insert depicts measurement technique. Ohmic pads are separated by 6.2 mm. Dc sheet resistance prior to laser processing is 2 MΩ/□.

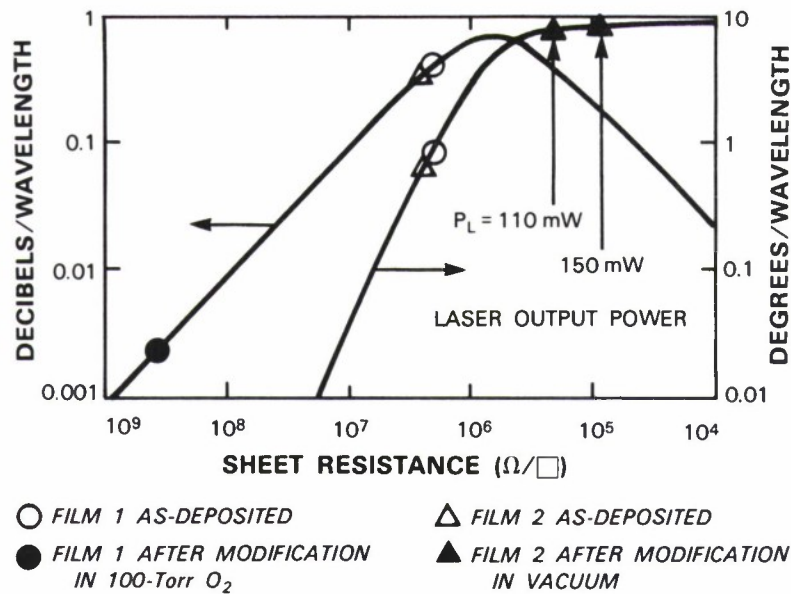


Figure 5-4. Calculated attenuation and phase shift of a SAW as a function of RF resistivity of a massless thin film deposited on  $YZ\text{-LiNbO}_3$  and measured properties of cermet films. Dc resistance of Film 1 is indicated; of Film 2 is inferred from acoustic properties.

An indication of the stability of the processed cermet is provided by its resistance to change with additional processing by the laser. Films initially modified in  $O_2$  or a vacuum showed no apparent change when an attempt was made to reconvert these films in a vacuum or  $O_2$ , respectively. Localized heating to  $200^\circ\text{C}$  of the  $\text{LiNbO}_3$  surface by the irradiated film is estimated.

In summary, a laser photochemical process has been developed which reproducibly transforms conductive ( $2 \text{ M}\Omega/\square$ ) and highly acoustically attenuating ( $0.4 \text{ dB}/\lambda$ ) cermet films to insulating ( $>100 \text{ M}\Omega/\square$ ) and nonattenuating ( $0.01 \text{ dB}/\lambda$ ) films. The process is being applied for *in situ* amplitude trimming of SAW dispersive delay lines.

V.S. Dolat  
J.H.C. Sedlacek

### 5.3 LOW-PHASE-NOISE OSCILLATORS STABILIZED BY BULK-ACOUSTIC-WAVE HOLOGRAPHIC-GRATING RESONATORS

The resonator is the limiting factor in the design of low-phase-noise oscillators operating at frequencies between 1 and 10 GHz. Today, a standard method of producing such frequencies is to multiply the output of a low-frequency quartz-crystal oscillator whose fundamental frequency is between 10 and 100 MHz (Reference 5); however, the multiplication process introduces substantial additional phase noise. Furthermore, in quartz the bulk-acoustic-wave (BAW) propagation loss increases at higher frequencies so that the  $Q$  of the resonator is too small to provide good performance at high fundamental frequencies.

SAW technology<sup>6</sup> has been very successful at frequencies up to 1 GHz, but a combination of intrinsic propagation loss, surface-degradation effects, and fabrication difficulties make operation of SAW devices at frequencies much above 1 GHz difficult. Composite BAW resonators<sup>7</sup> employ thin piezoelectric films deposited on thick films or membranes of nonpiezoelectric material, but to date the reported  $Q$ s have been limited to a few thousand. Also under development are the high-overtone bulk-acoustic resonators (HBARs)<sup>8</sup> which use a piezoelectric film deposited on a substrate that is many wavelengths thick and has high acoustic  $Q$ . Quality factors of 30,000 have been reported and  $10^5$  potentially could be reached. A nonacoustic approach, the ceramic dielectric-resonator oscillator (DRO),<sup>9</sup> is quite promising at frequencies above 10 GHz, but to date only a limited amount of data has been published for operation between 1 and 10 GHz. Although these methods are under development, there is no well-established technology for producing small, high-performance, and relatively inexpensive frequency sources in the microwave region.

The use of holographic gratings to construct BAW resonators, the principles of operation, and possible  $Q$  values have been discussed in earlier reports.<sup>10</sup> To demonstrate the actual operation of these resonators and to measure the phase-noise performance, we have assembled bread-board oscillators using the circuit shown in Figure 5-5. The circuit oscillates at the frequency where the feedback-loop gain is  $>1$  and the phase shift is  $360^\circ$ . The bandpass filter is needed because, at frequencies far from the transducer resonance, the reflection coefficient from the transducer becomes large enough to cause stability problems.

Phase noise is the figure of merit used to characterize the short-term stability of an oscillator.<sup>11</sup> To measure the phase noise, two identical oscillators were built with matched BAW resonators. The oscillators were phase-locked in quadrature and the outputs mixed, lowpass filtered, amplified, and measured in a spectrum analyzer. Preliminary results for the phase-noise performance are shown in Figure 5-6. For comparison, the performance of a typical SAW oscillator is shown with the results which have been reported for HBAR devices. The BAW reflection-grating oscillator already has achieved very respectable performance.

Also shown in Figure 5-6 is a calculated curve which results from a simplified model for the single-sideband phase noise of a feedback oscillator.<sup>6</sup> From this model, the single-sideband noise power in a 1-Hz bandwidth, relative to the carrier power, is given by



$$\mathcal{L}(f) = 10 \log \left[ \frac{GFkT}{P_c} \left( 1 + \frac{f_o^2}{4Q^2f^2} \right) \right] \quad (5-1)$$

where  $\mathcal{L}(f)$  is in dBc/Hz,  $P_c$  is the oscillator power,  $G$  the loop gain,  $F$  the amplifier-noise figure,  $f$  the offset frequency,  $Q$  the resonator quality factor, and  $f_o$  the oscillator fundamental frequency. Flicker noise was ignored.

Equation (5-1) is plotted in Figure 5-6 for a  $G$  of 47 dB,  $F$  of 4 dB,  $P_c$  of 17 dBm, and  $Q$  of  $1.2 \times 10^4$  to gain some insight into our measurements, which, as is evident, agree well with the simplified expression. The 47-dB gain is needed to overcome a device insertion loss of 27 dB, hybrid loss of 7 dB, filter loss of 5 dB, and phase-shifter loss of 5 dB. Note that there are no free parameters. This agreement is quite encouraging because Equation (5-1) contains several parameters which can be improved significantly to yield even lower phase noise. For example,  $Q$  can be raised by a factor between 3 and 10, device insertion loss can be lowered about 10 dB, improved loop components (such as phase shifters and hybrids) can be used to save another 10 dB of loop gain, and oscillator power can be increased by as much as 10 dB. The dot-dash line in Figure 5-6 is plotted for a  $G$  of 27 dB,  $F$  of 4 dB,  $P_c$  of 27 dBm, and  $Q$  of  $3 \times 10^4$ .

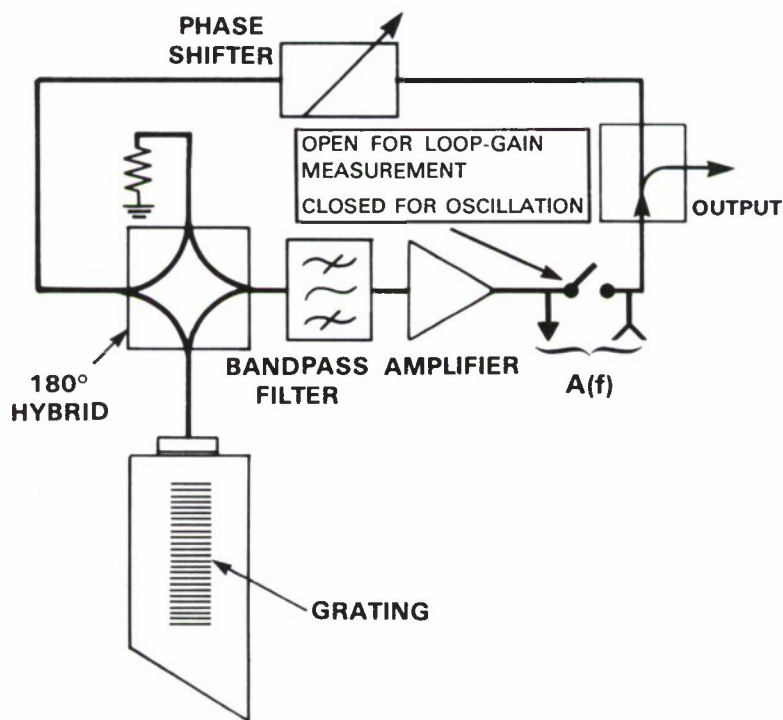


Figure 5-5. Schematic of circuit to demonstrate BAW-resonator-stabilized oscillator. Configuration used to measure open-loop response is indicated.

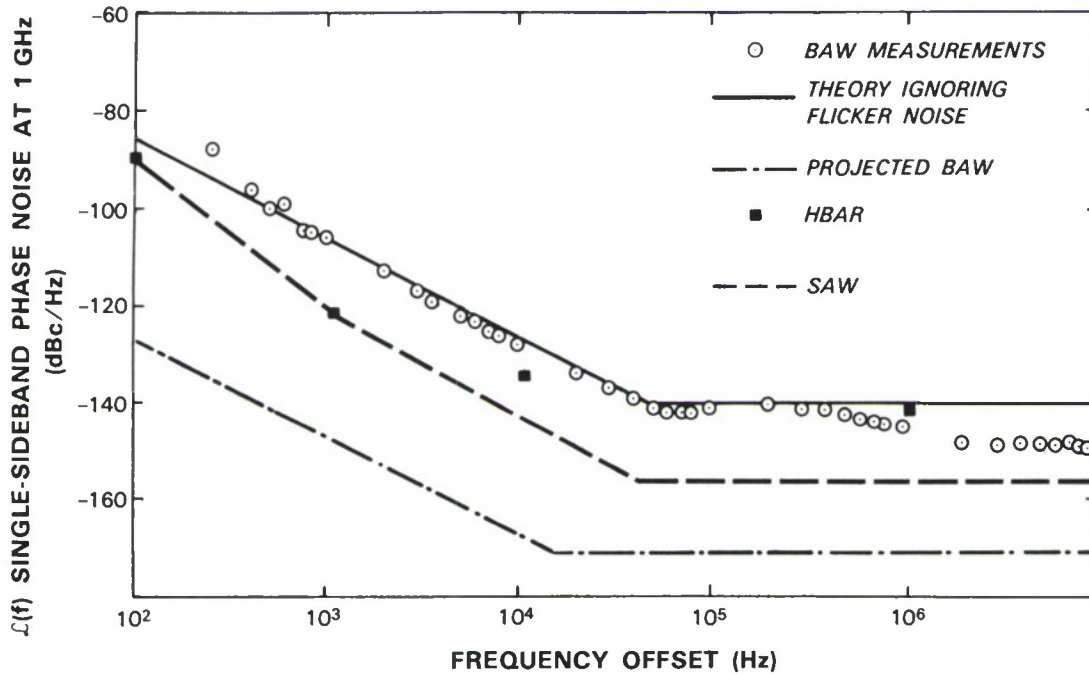


Figure 5-6. Results of preliminary measurements of phase noise in BAW-resonator-stabilized oscillators. Shown is noise in a typical SAW oscillator multiplied to 1-GHz operation and noise for HBAR devices. Also shown is a theoretical curve which ignores flicker-noise contributions from either circuit or device, obtained by using Equation (5-1) with  $G = 47$  dB,  $F = 4$  dB,  $P_c = 17$  dBm, and  $Q = 1.2 \times 10^4$ . Agreement between theory and experiment is excellent. Bottom curve shows projected noise with improvements discussed in text, using Equation (5-1) with  $G = 27$  dB,  $F = 4$  dB,  $P_c = 27$  dBm, and  $Q = 3 \times 10^4$ .

Equation (5-1) is useful because it contains an analytic expression in which one easily can see the influence of the various parameters on the resulting phase noise. It is useful also, however, to develop a more detailed model so that performance can be calculated more exactly. We have done this by extending the standard model of a feedback oscillator as presented in Reference 11 to include the details of the measured open-loop response as shown in Figures 5-5 and 5-7. Oscillator output is considered amplified thermal noise which is fed back through the acoustic resonator. The calculation predicts an output power spectral density

$$P(f) = \frac{FGkT}{1 + A^2 - 2A \cos \phi} \quad (5-2)$$

where  $A(f)e^{j\phi(f)}$  is the measured open-loop frequency response, as defined in Figure 5-5.

The results of these calculations are shown in Figure 5-8 and compared with phase-noise measurements for a pair of oscillators for which detailed measurements of the loop response have

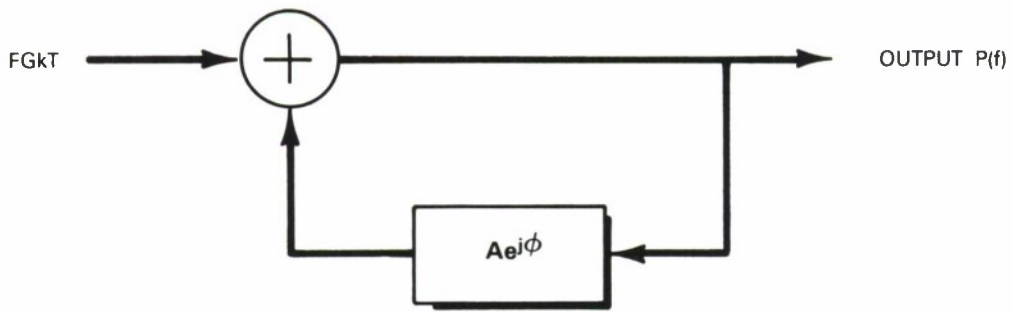


Figure 5-7. Standard feedback-oscillator model used to calculate phase noise. To measure open-loop frequency response  $Ae^{j\phi}$ , loop is broken as shown in Figure 5-5 and a test signal injected.

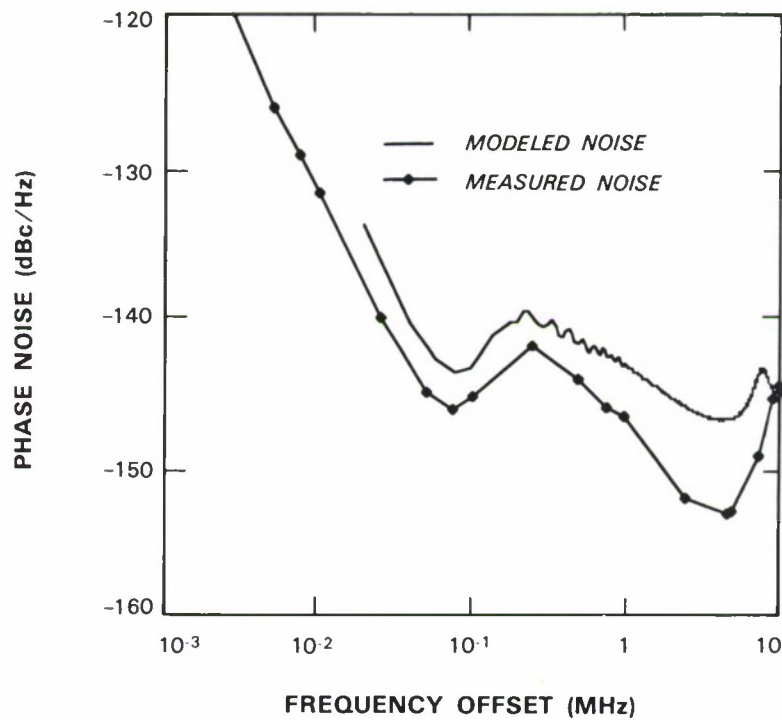


Figure 5-8. Results of model calculations of phase noise compared with measurements, using model of Figure 5-7 and measured open-loop response. Agreement is within measurement accuracy of  $\pm 4$  dBc/Hz.

been made. This pair of oscillators is different from that which yielded the results shown in Figure 5-6, although the responses were generally the same. Agreement is excellent and easily within the measurement accuracy, which we have estimated to be about  $\pm 4$  dBc/Hz. The details of the curve reflect the actual response of the resonators. The local maximum at  $\sim 300$ -kHz offset results from the bulk-wave-transducer reflection coefficient.

All the experimental results to date, for reasons of expediency, have been obtained with operation between 1 and 1.5 GHz. Extension to higher frequencies is possible.<sup>10</sup> The fundamental processes of hologram formation support very high resolution and do not limit the frequency of operation in any way. The largest impediment to operation at higher frequencies is the BAW transducer. We plan to demonstrate higher-frequency operation using deposited ZnO thin-film transducers.

We have presented experimental results for an important new technology of BAW devices operating at frequencies above 1 GHz, demonstrating a prototype resonator with performance comparable to the present state-of-the-art SAW and BAW devices. We have developed a model which accurately predicts performance and also have discussed methods by which considerable improvement in phase-noise performance can be achieved. Operating frequencies as high as 10 GHz should be realizable.

D.E. Oates  
J.Y. Pan



## REFERENCES

1. J.P. Sage, K.E. Thompson, and R.S. Withers, AIP Conference Proceedings, Vol. 151, *Neural Networks for Computing*, Snowbird, Utah, 13-16 April 1986, p.381.
2. R.S. Withers, R.W. Ralston, and E. Stern, IEEE Electron Device Lett. **EDL-1**, 42 (1980), DDC AD-A096617.
3. Solid State Research Report, Lincoln Laboratory, MIT (1985:1), p.51, DTIC AD-A160922.
4. A.C. Anderson, V.S. Dolat, and W.T. Brogan, *1980 Ultrasonics Symposium Proceedings* (IEEE, New York, 1980), p. 442, DTIC AD-A102966.
5. E.A. Gerber, T. Lukaszek, and A. Ballato, IEEE Trans. Microwave Theory Tech. **MTT-34**, 1002 (1986).
6. T.E. Parker, *Precision Frequency Control*, Vol. 2, E.A. Gerber and A. Ballato, Eds. (Academic Press, Orlando, 1985), p. 66.
7. T.W. Grudkowski, J.G. Black, T.M. Reeder, D.E. Cullen, and R.A. Wagner, *1980 Ultrasonics Symposium Proceedings* (IEEE, New York, 1980), p. 829.
8. J.T. Haynes, M.S. Buchalter, R.A. Moore, H.L. Salvo, S.G. Shepard, and B.R. McAvoy, *1985 MTT-S Digest* (IEEE, New York, 1985), p. 243.
9. G.D. Alley and H.C. Wang, IEEE Trans. Microwave Theory Tech. **MTT-17**, 969 (1979).
10. Solid State Research Report, Lincoln Laboratory, MIT (1986:2), p. 62.
11. W.P. Robbins, *Phase Noise in Signal Sources* (Peter Peregrinus Ltd., London, 1982).

UNCLASSIFIED

SECURITY CLASSIFICATION OF THIS PAGE

## REPORT DOCUMENTATION PAGE

1a. REPORT SECURITY CLASSIFICATION Unclassified			1b. RESTRICTIVE MARKINGS			
2a. SECURITY CLASSIFICATION AUTHORITY			3. DISTRIBUTION/AVAILABILITY OF REPORT Approved for public release; distribution unlimited.			
2b. DECLASSIFICATION/DOWNGRADING SCHEDULE						
4. PERFORMING ORGANIZATION REPORT NUMBER(S) 1987:1			5. MONITORING ORGANIZATION REPORT NUMBER(S) ESD-TR-86-176			
6a. NAME OF PERFORMING ORGANIZATION Lincoln Laboratory, MIT		6b. OFFICE SYMBOL (If applicable)		7a. NAME OF MONITORING ORGANIZATION Electronic Systems Division		
6c. ADDRESS (City, State, and Zip Code) P.O. Box 73 Lexington, MA 02173-0073			7b. ADDRESS (City, State, and Zip Code) Hanscom AFB, MA 01731			
8a. NAME OF FUNDING/SPONSORING ORGANIZATION Air Force Systems Command, USAF		8b. OFFICE SYMBOL (If applicable)		9. PROCUREMENT INSTRUMENT IDENTIFICATION NUMBER F19628-85-C-0002		
8c. ADDRESS (City, State, and Zip Code) Andrews AFB Washington, DC 20334			10. SOURCE OF FUNDING NUMBERS			
			PROGRAM ELEMENT NO. 63250F	PROJECT NO. 649L	TASK NO.	WORK UNIT ACCESSION NO.
11. TITLE (Include Security Classification) Solid State Research						
12. PERSONAL AUTHOR(S) Alan L. McWhorter						
13a. TYPE OF REPORT Quarterly Technical Report		13b. TIME COVERED FROM 1 Nov 86 TO 31 Jan 87		14. DATE OF REPORT (Year, Month, Day) 1987, February 15		15. PAGE COUNT 90
16. SUPPLEMENTARY NOTATION None						
17. COSATI CODES			18. SUBJECT TERMS (Continue on reverse if necessary and identify by block number)			
FIELD	GROUP	SUB-GROUP	solid state devices      ion implantation      charge-coupled devices			
			quantum electronics      optical modulators      microwave semiconductor			
			materials research      lasers      devices			
			microelectronics      quantum-well effects      superconductors			
			analog device technology      nonlinear optics      neural networks			
19. ABSTRACT (Continue on reverse if necessary and identify by block number)						
<p>This report covers in detail the solid state research work of the Solid State Division at Lincoln Laboratory for the period 1 November 1986 through 31 January 1987. The topics covered are Solid State Device Research, Quantum Electronics, Materials Research, Microelectronics, and Analog Device Technology. Funding is provided primarily by the Air Force, with additional support provided by the Army, DARPA, Navy, SDIO, NASA, and DOE.</p>						
20. DISTRIBUTION/AVAILABILITY OF ABSTRACT <input type="checkbox"/> UNCLASSIFIED/UNLIMITED <input checked="" type="checkbox"/> SAME AS RPT. <input type="checkbox"/> DTIC USERS			21. ABSTRACT SECURITY CLASSIFICATION Unclassified			
22a. NAME OF RESPONSIBLE INDIVIDUAL Maj. Thomas J. Alpert, USAF			22b. TELEPHONE (Include Area Code) (617) 863-5500, X-2330		22c. OFFICE SYMBOL ESD/TML	